

# Reactive Species and Reaction Pathways for the Oxidative Cleavage of 4-Octene and Oleic Acid with H<sub>2</sub>O<sub>2</sub> over Tungsten Oxide Catalysts

Danim Yun, E. Zeynep Ayla, Daniel T. Bregante, and David W. Flaherty\*



Cite This: *ACS Catal.* 2021, 11, 3137–3152



Read Online

ACCESS |



Metrics & More



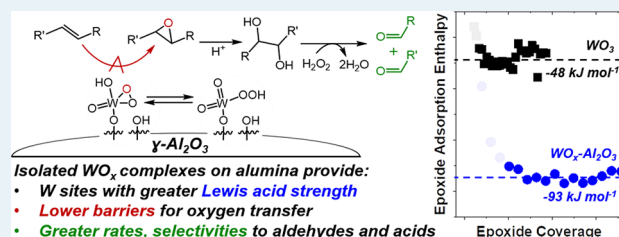
Article Recommendations



Supporting Information

**ABSTRACT:** Oxidative cleavage of carbon–carbon double bonds (C=C) in alkenes and fatty acids produces aldehydes and acids valued as chemical intermediates. Solid tungsten oxide catalysts are low cost, nontoxic, and selective for the oxidative cleavage of C=C bonds with hydrogen peroxide (H<sub>2</sub>O<sub>2</sub>) and are, therefore, a promising option for continuous processes. Despite the relevance of these materials, the elementary steps involved and their sensitivity to the form of W sites present on surfaces have not been described. Here, we combine in situ spectroscopy and rate measurements to identify significant steps in the reaction and the reactive species present on the catalysts and examine differences between the kinetics of this reaction on isolated W atoms grafted to alumina and on those exposed on crystalline WO<sub>3</sub> nanoparticles. Raman spectroscopy shows that W–peroxo complexes (W–(η<sup>2</sup>-O<sub>2</sub>)) formed from H<sub>2</sub>O<sub>2</sub> react with alkenes in a kinetically relevant step to produce epoxides, which undergo hydrolysis at protic surface sites. Subsequently, the CH<sub>3</sub>CN solvent deprotonates diols to form alpha-hydroxy ketones that react to form aldehydes and water following nucleophilic attack of H<sub>2</sub>O<sub>2</sub>. Turnover rates for oxidative cleavage, determined by in situ site titrations, on WO<sub>x</sub>–Al<sub>2</sub>O<sub>3</sub> are 75% greater than those on WO<sub>3</sub> at standard conditions. These differences reflect the activation enthalpies (ΔH<sup>‡</sup>) for the oxidative cleavage of 4-octene that are much lower than those for the isolated WO<sub>x</sub> sites (36 ± 3 and 60 ± 6 kJ·mol<sup>-1</sup> for WO<sub>x</sub>–Al<sub>2</sub>O<sub>3</sub> and WO<sub>3</sub>, respectively) and correlate strongly with the difference between the enthalpies of adsorption for epoxyoctane (ΔH<sub>ads,epox</sub>), which resembles the transition state for epoxidation. The WO<sub>x</sub>–Al<sub>2</sub>O<sub>3</sub> catalysts mediate oxidative cleavage of oleic acid with H<sub>2</sub>O<sub>2</sub> following a mechanism comparable to that for the oxidative cleavage of 4-octene. The WO<sub>3</sub> materials, however, form only the epoxide and do not cleave the C–C bond or produce aldehydes and acids. These differences reflect the distinct site requirements for these reaction pathways and indicate that acid sites required for diol formation are strongly inhibited by oleic acids and epoxides on WO<sub>3</sub> whereas the Al<sub>2</sub>O<sub>3</sub> support provides sites competent for this reaction and increase the yield of the oxidative cleavage products.

**KEYWORDS:** *unsaturated fatty acids, in situ spectroscopy, site titrations, kinetics, isothermal titration calorimetry*



## 1. INTRODUCTION

Oxidative cleavage of the double bonds within alkenes and unsaturated fatty acids (UFA) provides pathways to reactive aldehyde, acid, and diacid intermediates useful for chemical synthesis. For example, nonanal, azelaic acid, azelaic acid, and pelargonic acid form by oxidative cleavage of oleic acid, and these medium chain length saturated aldehydes and acids find use in the preparation of polymers (Nylon-6:9), plasticizers, adhesives, and lubricants.<sup>1–4</sup> Ozonolysis leads among current industrial methods for oxidative cleavage due to its high selectivity,<sup>5</sup> however, this chemistry involves the use of hazardous compounds (O<sub>3</sub>, metal-free process) and carries high capital costs and significant energy demands.<sup>6–8</sup> These drawbacks motivate the research and development of alternative chemistries of oxidative cleavage.

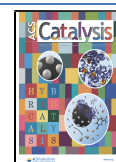
Reactions of transition metal-based catalysts with hydrogen peroxide (H<sub>2</sub>O<sub>2</sub>), a comparably benign oxidant, offer a replacement for ozonolysis. Soluble molecular complexes that contain Fe,<sup>1,9</sup> Os,<sup>10,11</sup> Co,<sup>12</sup> Mo,<sup>13</sup> W,<sup>2,13–15</sup> or Ru<sup>16–18</sup>

activate H<sub>2</sub>O<sub>2</sub> and give significant turnover numbers and yield for the oxidative cleavage of alkenes and unsaturated fatty acids. Among these elements, tungsten-based catalysts, including WO<sub>3</sub>, W-based polyoxometallates, and tungstic acid, provide low toxicity and cost,<sup>19</sup> high stability compared to Fe, Co, and Mo complexes,<sup>1</sup> and appreciable rates for hydrogen peroxide-mediated oxidation.<sup>20,21</sup> Oguchi et al.<sup>22</sup> reported that reactions of cyclohexene with stoichiometric quantities of H<sub>2</sub>O<sub>2</sub> over tungstic acid (H<sub>2</sub>WO<sub>4</sub>, with a molar ratio of cyclohexene to H<sub>2</sub>WO<sub>4</sub> of ~2) or tungstophosphoric acid (H<sub>3</sub>PW<sub>12</sub>O<sub>40</sub>, with a molar ratio of cyclohexene to H<sub>3</sub>PW<sub>12</sub>O<sub>40</sub> equal to ~25) give adipic acid yields of 62% and

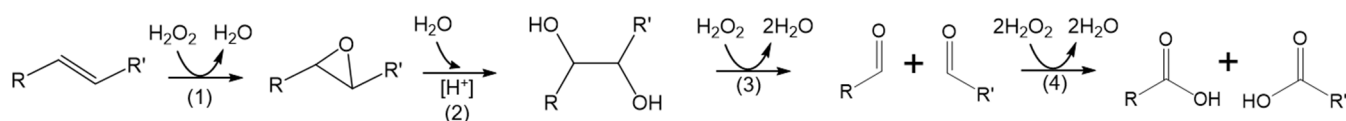
Received: December 8, 2020

Revised: January 31, 2021

Published: February 24, 2021



**Scheme 1. Commonly Proposed Stoichiometric Reactions Involved in the Oxidative Cleavage of Unsaturated Carbon–Carbon Bonds in Linear Alkenes**



50%, respectively (*tert*-butanol, 356 K, 24 h). Turnwald et al.<sup>13</sup> reported the oxidative cleavage of neat oleic acid with an excess of H<sub>2</sub>O<sub>2</sub> over peroxy-tris(cetylpyridinium) tungstophosphate (H<sub>2</sub>O<sub>2</sub>-activated ( $\pi$ -C<sub>5</sub>H<sub>5</sub>N<sup>+</sup>(CH<sub>2</sub>)<sub>15</sub>CH<sub>3</sub>)<sub>3</sub>(PW<sub>12</sub>O<sub>40</sub>)<sup>3-</sup> with a molar ratio of oleic acid to catalyst of 77), which gave a 57% yield of azelaic acid and nonanoic acid (363 K, 5 h); however, the catalyst could not be regenerated. In comparison, the cesium form of the same catalyst (peroxy-tri(cesium)12-tungstophosphate, H<sub>2</sub>O<sub>2</sub>-activated Cs<sub>3</sub>(PW<sub>12</sub>O<sub>40</sub>)<sup>3-</sup>, molar ratio of oleic acid to catalyst of 77) was stable but provided a lower yield of azelaic acid (28%, 363 K, 10 h).<sup>13</sup> The sodium salt of tungstic acid (Na<sub>2</sub>WO<sub>4</sub>) was used by Noyori et al.<sup>23</sup> to convert cyclohexene to adipic acid with a high yield (93%, molar ratio of cyclohexene to catalyst equal to 100, neat cyclohexene, 363 K, 8 h) when combined with a phase transfer catalyst (PTC, (CH<sub>3</sub>(*n*-C<sub>8</sub>H<sub>17</sub>)<sub>3</sub>N)HSO<sub>4</sub>, molar ratio of PTC to Na<sub>2</sub>WO<sub>4</sub> of 1). Although these prior studies demonstrate that W-based homogeneous complexes are competent catalysts for oxidative cleavage reactions with H<sub>2</sub>O<sub>2</sub>, the solubility of these complexes introduces significant challenges for large-scale processes. Consequently, several groups have examined heterogeneous tungstate catalysts for liquid-phase oxidative cleavage reactions with H<sub>2</sub>O<sub>2</sub>, yet reported selectivities are much lower than homogeneous W catalyst. Silica-supported WO<sub>3</sub> only yields 30% azelaic acid and nonanoic acid from oleic acid.<sup>6</sup> WO<sub>3</sub> catalyst promoted with Na<sub>2</sub>SnO<sub>3</sub> gives a 90% yield of the desired acids (at 100% conversion) from oxidative cleavage of oleic acid; however, WO<sub>3</sub> in the absence of cocatalyst is much less effective (60% acid yield).<sup>24</sup>

The reasons for the lower rates and selectivities for oxidative cleavage over solid tungstate catalysts remain uncertain due, in part, to a lack of knowledge regarding the elementary steps involved in oxidative cleavage reactions on these materials and their kinetic relevance, the identity of the reactive species, and the form of the active W complexes. Scheme 1 shows the sequence of stoichiometric reactions generally accepted for the H<sub>2</sub>O<sub>2</sub>-mediated oxidative cleavage of alkenes. Antonelli et al.<sup>25</sup> proposed that the reaction proceeds by epoxidation of the alkene followed by hydrolysis of the oxirane ring to yield the diol. Subsequently, deprotonation of the diol produces an alpha-hydroxy ketone intermediate susceptible to nucleophilic attack by H<sub>2</sub>O<sub>2</sub> that cleaves the C–C bond and forms aldehyde products. Finally, additional equivalents of H<sub>2</sub>O<sub>2</sub> oxidize the aldehydes to yield the carboxylic acids. Oxidative cleavage of unsaturated fatty acids likely involves similar steps as mechanisms for cyclo- or linear alkenes; however, the relative rates of these steps and therefore the distribution of the products may differ as a result of the terminal carboxylic acid function on the reactant and its impact on the prevailing intermediates bound to the active sites.<sup>1</sup> We are not aware of prior investigations that have measured and molecularly interpreted the effects of reactant concentrations on product formation rates for linear alkenes and unsaturated fatty acid oxidative cleavages over solid catalysts.

In addition, the structural heterogeneity among plausible active sites on many forms of solid tungstate catalysts complicates efforts to identify reactive intermediates. Prior work indicates that reactive tungsten–peroxy complexes (W–( $\eta^2$ -O<sub>2</sub>)) form by activation of H<sub>2</sub>O<sub>2</sub> on coordinatively unsaturated W atoms (e.g., tetrahedrally coordinated, isolated W atoms) as opposed to more highly coordinated W atoms within continuous tungstate domains.<sup>26–28</sup> Hammond et al.,<sup>29</sup> however, compared cyclooctene epoxidation rates upon WO<sub>3</sub> nanoparticles and W–Zn/SnO<sub>2</sub> catalysts and concluded that crystalline WO<sub>3</sub> is the most active and stable phase for H<sub>2</sub>O<sub>2</sub>-mediated epoxidation, not mono- or polytungstates.

Here, we examine reactive intermediates, reaction mechanisms, and the effects of the active site structure for the oxidative cleavage of 4-octene and oleic acid over supported and unsupported tungsten oxide catalysts. We synthesized WO<sub>x</sub> complexes on  $\gamma$ -Al<sub>2</sub>O<sub>3</sub> with varying extents of dispersion by surface grafting methods. Raman, UV–vis, and XRD indicate that this method forms materials that possess predominantly monomeric and dimeric WO<sub>x</sub> species at the lowest W surface coverages under the reaction conditions. A combination of kinetic measurements and in situ spectroscopy demonstrates that the surface chemistry and catalysis on these WO<sub>x</sub> sites resembles that of crystalline WO<sub>3</sub> nanoparticles; however, reaction rates and activation barriers differ significantly. In situ Raman and UV–vis spectroscopies suggest W–peroxide complexes (i.e., W–peroxy (W–( $\eta^2$ -O<sub>2</sub>))) and W–hydroperoxy (W–OOH) both participate in steps for oxidative cleavage and form by activation of H<sub>2</sub>O<sub>2</sub>-exposed W atoms. Rate measurements as functions of the concentrations of the organic substrates, H<sub>2</sub>O<sub>2</sub>, and the epoxide intermediates reveal that oxidative cleavage involves kinetically relevant epoxidation of the alkene on W–( $\eta^2$ -O<sub>2</sub>) and ring opening of the epoxide to form a diol on acidic sites (W–OOH). Subsequent steps that cleave the diol and yield aldehyde and acid products occur by reactions with the solvent (CH<sub>3</sub>CN) and H<sub>2</sub>O<sub>2</sub> in the liquid phase. The apparent activation enthalpies ( $\Delta H^\ddagger$ ) for oxidative cleavage of 4-C<sub>8</sub>H<sub>16</sub> on WO<sub>x</sub>–Al<sub>2</sub>O<sub>3</sub> are 24 kJ·mol<sup>-1</sup> lower than those on WO<sub>3</sub>, and the turnover rates on isolated WO<sub>x</sub> sites are 75% greater at standard reaction conditions. The differences between  $\Delta H^\ddagger$  on these catalysts correlate with differences in the Lewis acid strength of these active sites and their enthalpies of adsorption for the epoxide intermediate ( $\Delta H_{\text{ads,epox}}$ ) as measured by isothermal titration calorimetry (ITC). These comparisons suggest that the isolated W sites give greater turnover rates, particularly at lower reaction temperatures, because alumina-supported WO<sub>x</sub> species possess greater electronegativities, bind epoxide products more strongly, and stabilize kinetically relevant transition states more effectively than W atoms exposed to WO<sub>3</sub>. More consequential differences between turnover rates and selectivities were observed during oleic acid conversion over WO<sub>x</sub>–Al<sub>2</sub>O<sub>3</sub> and WO<sub>3</sub> catalysts. Particles of WO<sub>3</sub> mainly produce the epoxide of oleic acid, while isolated WO<sub>x</sub> sites give high selectivities for oxidative cleavage

**Table 1.** Characterization of  $X\text{-WO}_x\text{-Al}_2\text{O}_3$  Catalysts Including W Content as Mass Percentage Loading and Surface Coverage, Band Gaps, and Vibrational Modes That Involve  $\text{WO}_x$  under Dehydrated and Hydrated Conditions

sample	mass loading of W (%) <sup>a</sup>	areal density of W atoms ( $\text{W}\cdot\text{nm}^{-2}$ ) <sup>b</sup>	band gap (eV) <sup>c</sup>	vibrational modes of dehydrated $\text{WO}_x$ <sup>d</sup>	vibrational modes of $\text{WO}_x$ in situ <sup>e</sup>
0.03- $\text{WO}_x\text{-Al}_2\text{O}_3$	0.25	0.03	4.9	$\nu(\text{W}=\text{O})$	$\nu(\text{W}=\text{O}), \nu(\text{W}-\text{O}-\text{W}), \nu(\text{WO}_2)$
0.06- $\text{WO}_x\text{-Al}_2\text{O}_3$	0.51	0.06	4.9	$\nu(\text{W}=\text{O})$	$\nu(\text{W}=\text{O}), \nu(\text{W}-\text{O}-\text{W}), \nu(\text{WO}_2)$
0.1- $\text{WO}_x\text{-Al}_2\text{O}_3$	1.0	0.1	4.7	n.d. <sup>f</sup>	n.d. <sup>f</sup>
0.4- $\text{WO}_x\text{-Al}_2\text{O}_3$	3.6	0.4	4.6	$\nu(\text{W}=\text{O}), \delta(\text{O}-\text{W}-\text{O}), \nu(\text{W}-\text{O}-\text{Al}), \text{WO}_3$	$\nu(\text{W}=\text{O}), \nu(\text{W}-\text{O}-\text{W}), \nu(\text{WO}_2), \text{WO}_3$
0.9- $\text{WO}_x\text{-Al}_2\text{O}_3$	7.5	0.9	4.5	$\nu(\text{W}=\text{O}), \delta(\text{O}-\text{W}-\text{O}), \nu(\text{W}-\text{O}-\text{Al}), \text{WO}_3$	$\nu(\text{W}=\text{O}), \nu(\text{W}-\text{O}-\text{W}), \nu(\text{WO}_2), \text{WO}_3$

<sup>a</sup>Measured by EDXRF. <sup>b</sup>BET surface area calculated from the  $\text{N}_2$  adsorption–desorption isotherm. <sup>c</sup>Calculated from Tauc plots of DRUV–vis spectra. <sup>d</sup>Measured by in situ Raman under dry flowing helium (298 K, 101 kPa He) after dehydration (773 K, 1 h,  $20 \text{ cm}^3\cdot\text{min}^{-1}$ ). <sup>e</sup>Measured by in situ Raman under flowing solutions of  $\text{H}_2\text{O}_2$  and  $\text{CH}_3\text{CN}$  (0.5 M  $\text{H}_2\text{O}_2$ , 1.98 M  $\text{H}_2\text{O}$ , 313 K,  $1 \text{ cm}^3\cdot\text{min}^{-1}$ ). <sup>f</sup>Not determined.

products. These differences reflect the limited number of protons on the  $\text{WO}_3$  surface and strong inhibition of the active sites by the carboxylic acid and the epoxide intermediate, both of which contribute to low rates for diol formation and oxidative cleavage. An abundance of protons on the W sites ( $\text{W}-\text{OOH}$ ) of  $\text{WO}_x\text{-Al}_2\text{O}_3$  facilitates hydrolysis of the epoxide and gives higher turnover rates for aldehyde and acid production.

## 2. MATERIALS AND METHODS

**2.1. Catalyst Synthesis.** Two forms of tungsten oxide catalysts were used in this work. Disperse W atoms were prepared on the surface of mesoporous alumina by grafting organotungsten complexes.<sup>30</sup> Aluminum oxide ( $\gamma\text{-Al}_2\text{O}_3$ , Sigma-Aldrich; 3.8 nm pores,  $364 \text{ m}^2\cdot\text{g}^{-1}$ ) was calcined in flowing air (Airgas, Ultra Zero grade) at 823 K for 6 h with the intent to remove organic residues and moisture. The cooled solid ( $\sim 1 \text{ g}$ ) was added to chloroform ( $120 \text{ cm}^3$ ;  $\text{CHCl}_3$ , TCI Chemical,  $\geq 99.0\%$ ) within a two-neck round-bottom flask under Ar (Airgas, 99.999%) flow in a glass air-free apparatus. The mixture was stirred for 0.5 h (300 rpm,  $\sim 295 \text{ K}$ ), after which bis(cyclopentadienyl)tungsten dichloride ( $(\text{C}_5\text{H}_5)_2\text{WCl}_2$ , Alfa Aesar, 99%) was added as a dry powder into a suspension of alumina in  $\text{CHCl}_3$ . The mixture was stirred under continuous Ar purge for 0.5 h. Then 3 equiv of triethylamine ( $(\text{C}_2\text{H}_5)_3\text{N}$ , Sigma-Aldrich, 99.5%) was added to the mixture to deprotonate the surface hydroxyls and adsorb  $(\text{C}_5\text{H}_5)_2\text{WCl}_2$ . The mixture was stirred for another 12 h. Subsequently, the solids were filtered, dried, and calcined at 823 K for 6 h in flowing air ( $100 \text{ cm}^3\cdot\text{min}^{-1}$ ; Airgas, Ultra Zero grade) to form tungsten oxide complexes ( $\text{WO}_x$ ) on the alumina. The resulting  $\text{WO}_x\text{-Al}_2\text{O}_3$  materials were characterized (vide infra) and denoted by the areal density of W atoms on the  $\text{Al}_2\text{O}_3$  surface ( $X\text{-WO}_x\text{-Al}_2\text{O}_3$ , where  $X$  is the number of W atoms per square nanometer ( $\text{W}\cdot\text{nm}^{-2}$ )). Tungsten oxide nanoparticles ( $\text{WO}_3$ ) were purchased (US Research Nanomaterials, US3538, 60 nm mean diameter) and used as received.

**2.2. Ex Situ Catalyst Characterization.** Adsorption and desorption isotherms of  $\text{N}_2$  were performed using a Micrometrics 3Flex analyzer and SmartVac degasser. Catalyst ( $< 50 \text{ mg}$ ) was loaded into a glass vessel and heated under vacuum to desorb water and organic residues. The degassed sample was weighed, and then the isotherms were obtained. The  $\text{N}_2$  adsorption–desorption isotherm of the  $\gamma\text{-Al}_2\text{O}_3$  calcined at 823 K for 6 h shows a type IV isotherm with H1-type

hysteresis. The total surface areas of these samples were determined to be  $281 \text{ m}^2\cdot\text{g}^{-1}$  using the BET method. The  $\text{N}_2$  adsorption–desorption isotherm of the  $\text{WO}_3$  nanoparticles exhibits hysteresis loops at 0.9–1.0 relative pressure due to the textural porosity of the nanoparticles, and the BET surface area of the  $\text{WO}_3$  nanoparticles was found to be  $11 \text{ m}^2\cdot\text{g}^{-1}$ .

Energy-dispersive X-ray fluorescence (EDXRF) was conducted to determine the composition of the synthesized catalysts (Table 1). Powder samples were loaded into the He-purged chamber of the spectrometer (EDX-7000, Shimadzu) and scanned from 0 to 30 keV.

The dispersity of the W atoms of  $X\text{-WO}_x\text{-Al}_2\text{O}_3$  was examined indirectly through diffuse reflectance UV–vis (DRUV–vis) spectroscopy. The spectra of samples diluted in magnesium oxide ( $\text{MgO}$ ,  $\geq 99.99\%$ , Sigma-Aldrich) were collected between 200 and 800 nm using a UV–vis spectrophotometer (Varian Cary, 5G) and referenced to diluent ( $\text{MgO}$ ). The measured reflectance spectra were transformed to the corresponding absorption spectra by applying the Kubelka–Munk function ( $F(R_\infty)$ ),<sup>31</sup> defined as

$$F(R_\infty) = \frac{(1 - R_\infty)^2}{2R_\infty} \quad (1)$$

where  $R_\infty$  represents the reflectance of an infinitely thick specimen and is obtained from the ratio of the sample reflectance to that of the standard ( $R_{\text{sample}}/R_{\text{standard}}$ ). Using the Tauc method to examine direct electron transitions,<sup>32,33</sup>  $F(R)$  is recast within the following linearized form

$$(F(R_\infty)h\nu)^2 = B(h\nu - E_g) \quad (2)$$

where  $h$  is the Planck constant,  $\nu$  is the photon frequency,  $E_g$  is the band gap energy of the samples, and  $B$  is a constant. Figure S3 shows the Kubelka–Munk absorbances of  $X\text{-WO}_x\text{-Al}_2\text{O}_3$  as a function of a photon energy (i.e., Tauc plot). The band gap energies were determined by the  $x$ -axis intersection point of the linear fit of the Tauc plot (Table 1 and Figure 1).

X-ray diffraction (XRD) patterns of the catalysts were obtained with a diffractometer (Bruker, D8 Advance) operating at 40 kV and 40 mA using Cu  $K\alpha$  radiation ( $1.5406 \text{ \AA}$ ). The samples were scanned in the  $2\theta$  range of  $20\text{--}80^\circ$  to examine the crystallinity of tungsten oxide structures (Figure S5).

**2.3. In Situ Raman and UV–vis Spectroscopy.** In situ Raman spectroscopy was used to examine the structure of the tungsten oxide domains in the dehydrated catalysts and the reactive species formed by contact with aqueous  $\text{H}_2\text{O}_2$

solutions. Raman spectra of the dehydrated catalysts were obtained from catalyst pellets placed in an environmentally controlled high-temperature cell reactor (Linkam, CCR1000). Before analysis, the catalysts were dehydrated at 823 K for 1 h in flowing O<sub>2</sub> (Airgas, ultrahigh purity, 20 cm<sup>3</sup> min<sup>-1</sup>) to desorb the adsorbed moisture. The spectra were collected after cooling the catalyst to room temperature in flowing O<sub>2</sub> gas (20 cm<sup>3</sup> min<sup>-1</sup>). Spectra were acquired with a Raman spectrometer (Renishaw, inVia) equipped with a 532 nm laser that was less than 41 mW·μm<sup>-2</sup> at the catalyst surface. The power density was measured directly using a portable power meter (Gentec-EO, PRONTO-SI). Experimental spectra represent the average of 1000 accumulations with 0.1 s per accumulation.

The Raman spectra of the catalysts under the reaction conditions were taken within a custom liquid flow cell. The pelletized catalysts were placed in this cell, immersed in flowing acetonitrile solutions (CH<sub>3</sub>CN, Fischer Chemicals, HPLC grade), and heated to 313 K. Steady-state spectra of the reactive intermediates were collected (0.1 s per accumulation, 1000 accumulations) in flowing solutions of H<sub>2</sub>O<sub>2</sub> and CH<sub>3</sub>CN (0.5 M H<sub>2</sub>O<sub>2</sub>, 1.98 M H<sub>2</sub>O, 313 K) delivered by an HPLC pump (SSI, LS Class; 1 cm<sup>3</sup> min<sup>-1</sup>). Spectra were acquired using a 532 nm laser with areal power density (5.2 mW·μm<sup>-2</sup> for X-WO<sub>x</sub>-Al<sub>2</sub>O<sub>3</sub> and 0.2 mW·μm<sup>-2</sup> for WO<sub>3</sub>).

In situ UV-vis spectra were collected using a 45° diffuse reflection probe (Avantes, solarization-resistant fibers) coupled to a fiber-optic spectrometer (Avantes, AvaFast 2048) with a compact deuterium-halogen light source (Avantes, AvaLight-DHc). The pelletized catalyst was loaded into a similar liquid flow cell as used for Raman spectra but equipped with a sealed port to admit the diffuse reflectance probe. The sample was contacted with flowing aqueous CH<sub>3</sub>CN (1.98 M H<sub>2</sub>O in CH<sub>3</sub>CN, 1 cm<sup>3</sup> min<sup>-1</sup>) and heated to 313 K while continuously scanning. Background spectra were obtained when the system reached steady state. The spectra of the reactive species were collected when samples contacted flowing H<sub>2</sub>O<sub>2</sub> solutions (0.5 M H<sub>2</sub>O<sub>2</sub>, 1.98 M H<sub>2</sub>O in CH<sub>3</sub>CN, 1 cm<sup>3</sup> min<sup>-1</sup>) at 313 K, and the system was allowed to reach steady state once more. Subsequently, the solution was switched to pure CH<sub>3</sub>CN (1 cm<sup>3</sup> min<sup>-1</sup>) to determine if the H<sub>2</sub>O<sub>2</sub>-activated species on these catalysts form reversibly. All UV-vis spectra of H<sub>2</sub>O<sub>2</sub>-derived intermediates represent the difference between the experimental spectrum (i.e., sample within aqueous H<sub>2</sub>O<sub>2</sub> solutions) and the background spectrum obtained within aqueous CH<sub>3</sub>CN in the absence of H<sub>2</sub>O<sub>2</sub>.

**2.4. Catalytic Reaction Rate Measurements.** Rates for oxidative cleavage of oleic acid (C<sub>18</sub>H<sub>34</sub>O<sub>2</sub>, TCI Chemical, >99%) and 4-octene (*trans*-4-C<sub>8</sub>H<sub>16</sub>, Sigma-Aldrich, 98%) were measured within batch reactors (100 cm<sup>3</sup>, three-neck round-bottom flasks) equipped with reflux condensers. The organic reactant was combined with hexane (an internal standard for GC analysis, C<sub>6</sub>H<sub>14</sub>, Sigma-Aldrich, ≥95%) and the catalyst (30–100 mg) and added to CH<sub>3</sub>CN. The mixture was heated to the desired temperature (313–343 K) and stirred at 700 rpm for 0.5 h. The reaction was initiated by adding the necessary amount of aqueous H<sub>2</sub>O<sub>2</sub> (Fischer Chemicals, 30% in H<sub>2</sub>O). Aliquots (~0.8 cm<sup>3</sup>) of the reaction solution were extracted as a function of reaction time using a syringe equipped with a filter (0.05 μm, polystyrene for WO<sub>3</sub>, 0.22 μm, polypropylene for X-WO<sub>x</sub>-Al<sub>2</sub>O<sub>3</sub>) to separate the catalyst particles from the reaction solution. Analogous approaches were used to determine the reaction rates for epoxide ring opening and the oxidative cleavage of diols. The

aliquots were analyzed using a gas chromatograph (Agilent 7890A) equipped with a flame ionization detector (FID). Reactants and products were separated in a column (HP-INNOWax, 30 m × 0.53 mm i.d., 1.0 μm film thickness). Peaks within the gas chromatograms were identified by comparisons to mixtures of known standards and with a mass-selective detector (MSD, Agilent, 5975B) operating with electron ionization. The alkene conversion and product selectivity were calculated as follows

$$\text{alkene conversion (\%)} = \frac{\text{moles of alkene reacted}}{\text{moles of alkene fed}} \times 100$$

$$\text{selectivity (\%)} = \frac{\text{moles of C in product}}{\text{moles of C in all products}} \times 100$$

Analysis of pseudosteady-state turnover rates for oxidative cleavage as a function of reactant concentration is reported on the basis of moles of carbon within the products normalized by the number of active sites (Section 2.5) per unit time (i.e., (mol C)/(mol W·s)<sup>-1</sup>). Reactions of 4-octene with H<sub>2</sub>O<sub>2</sub> give selectivity to butanal of ~95% over both WO<sub>3</sub> and WO<sub>x</sub>-Al<sub>2</sub>O<sub>3</sub> catalysts at the reaction conditions and low conversions examined here. Therefore, moles of carbon within produced butanal are used to determine turnover rates for oxidative cleavage. Carbon balances for reactions with 4-octene are typically 85–95%. Reaction with oleic acid, however, gave different selectivities to epoxide (i.e., 8-(3-octyloxiran-2-yl)octanoic acid) and oxidative cleavage products (i.e., nonanal, nonanoic acid, 9-oxo-nonanoic acid, azelaic acid) over WO<sub>3</sub> and WO<sub>x</sub>-Al<sub>2</sub>O<sub>3</sub> catalysts. Over WO<sub>3</sub>, selectivity for epoxide is greater than 98% and selectivity for oxidative cleavage products is less than 2%. On the other hand, selectivity for oxidative cleavage products is greater than 80% over WO<sub>x</sub>-Al<sub>2</sub>O<sub>3</sub> catalyst. Turnover rates for oleic acid consumption were determined from the sum of the formation rates for all detected products (i.e., 8-(3-octyloxiran-2-yl)octanoic acid, nonanal, nonanoic acid, 9-oxo-nonanoic acid, and azelaic acid) over both catalysts. Carbon balances for reactions with oleic acid are 60–80% and are systematically lower than for reactions with 4-octene.

The concentration of H<sub>2</sub>O<sub>2</sub> was measured by colorimetric titration using a titrant solution which is an aqueous solution of CuSO<sub>4</sub> (8.3 mM, Fisher Chemicals, >98.6%), neocuproine (12 mM, Sigma-Aldrich, >98%), and ethanol (25% v/v, Decon Laboratories, 100%). The reaction solution was diluted to 1–10% v/v reaction solution with CH<sub>3</sub>CN. The diluted reaction solution (10 μL) was titrated with the titrant (0.2 cm<sup>3</sup>), and the absorbance at 454 nm was determined using a multi-detection microplate reader (BioTek, Synergy 2). The measured H<sub>2</sub>O<sub>2</sub> concentration values were used to calculate H<sub>2</sub>O<sub>2</sub> decomposition rates.

We carried out a hot filtration test for WO<sub>x</sub>-Al<sub>2</sub>O<sub>3</sub> catalyst to determine if active WO<sub>x</sub> species are leaching from the alumina support (Section S1.1). During a reaction, an aliquot of the reaction mixture (8 cm<sup>3</sup>) was taken by syringe at 30 min, the solid catalyst was filtered, and the liquid solution was transferred into a 20 cm<sup>3</sup> scintillation vial (700 rpm, 333 K). Aliquots were taken from the batch reactor and scintillation vial as a function of time, and concentrations of reactant and products were measured by gas chromatography. The concentrations of butanal do not change following filtration of the catalyst (Figure S1), which indicates that the active WO<sub>x</sub>

species do not leach from the alumina support and catalyze reactions in the solution.

$\text{WO}_x\text{-Al}_2\text{O}_3$  catalysts are stable and regenerable, which was established by conducting four subsequent batch reactions, each followed by an oxidative catalyst regeneration treatment (Section S1.2). Each batch reaction (5 mM 4- $\text{C}_8\text{H}_{16}$ , 0.1 M  $\text{H}_2\text{O}_2$ , 0.39 M  $\text{H}_2\text{O}$  in  $\text{CH}_3\text{CN}$ ) was conducted for 30 min. The used catalyst was separated from the reaction mixture by centrifugation at 400 rpm for 10 min. Then the recovered solid catalyst was dried at 338 K for 30 min and heated to 823 K for 6 h in flowing dry air to remove water and organic species. The W content of the regenerated catalyst was determined by EDXRF and compared to that of the fresh catalyst. The catalyst was then reused for the subsequent reaction. Figure S2 shows that the W content remained constant at  $0.50 \pm 0.006\%$  by weight throughout the course of the four reactions, and the turnover rate was consistently  $2.6 \pm 0.2$  (mmol C)(mol W s) $^{-1}$  for all four reactions. The consistency of these values demonstrates that the  $\text{WO}_x\text{-Al}_2\text{O}_3$  catalysts are stable under these reaction conditions.

**2.5. Active Site Titrations with Phenyl Phosphonic Acid.** The number of active sites in each catalyst was determined by in situ titrations with phenyl phosphonic acid (PPA, Sigma-Aldrich, 98%) during oxidative cleavage of 4- $\text{C}_8\text{H}_{16}$  (0.025 M 4- $\text{C}_8\text{H}_{16}$ , 0.1 M  $\text{H}_2\text{O}_2$ , 333 K) or oleic acid (0.1 M oleic acid, 0.5 M  $\text{H}_2\text{O}_2$ , 343 K). Briefly, the reactant (i.e., 4- $\text{C}_8\text{H}_{16}$  or oleic acid), the catalyst, hexane (an internal standard for GC analysis), and PPA were added to the  $\text{CH}_3\text{CN}$  solvent and stirred for 1 h. During this period, PPA adsorbs to the active sites of these catalysts, where PPA inhibits catalysis. The catalytic reaction was initiated by adding  $\text{H}_2\text{O}_2$ , and the initial reaction rates were determined as a function of the molar ratio of PPA to W atoms. The number of active sites for each catalyst was determined by extrapolating linear regions of these plots to the abscissa, which provides the number of PPA and the ratio of PPA to W atoms required to completely suppress catalysis. This analysis assumes that one PPA molecule occupies a single active site.

**2.6. Isothermal Titration Calorimetry.** The heat released upon 1,2-epoxyoctane adsorption onto W active sites was measured using an isothermal titration calorimeter (ITC) equipped with gold reference and sample cells (TA Instruments, NanoITC). Briefly, the tungsten oxide catalyst (40–80 mg of  $\text{WO}_x\text{-Al}_2\text{O}_3$  or  $\text{WO}_3$ ) was suspended in 500  $\mu\text{L}$  of  $\text{CH}_3\text{CN}$  (Sigma-Aldrich, 99.8%) by sonicating for 20 min, and the suspension was used to fill the sample cell of the calorimeter. The residual suspension was dried in the loading vessel at 373 K for 12 h, and the weight difference after filling the sample cell was used to determine the amount of catalyst loaded into the calorimeter. The reference cell was filled with neat  $\text{CH}_3\text{CN}$ .

The titration syringe was filled with a solution of 1,2-epoxyoctane (0.01 M; 1,2- $\text{C}_8\text{H}_{16}\text{O}$ , Sigma-Aldrich, 98%) in  $\text{CH}_3\text{CN}$ , and the system was thermally equilibrated prior to the start of the experiment. Injections (1  $\mu\text{L}$ ) were made at regular intervals (300 s) in each experiment, which allowed the system to return to the baseline heating rate prior to the subsequent injection. Data analysis was performed with the NanoAnalyze software package (TA Instruments). The number of W sites available for titration was determined using the mass of the catalyst in the sample cell and the number of W active sites per gram (quantified by phenyl phosphonic acid titrations). Heats of adsorption are presented

as a function of the fractional coverage of 1,2- $\text{C}_8\text{H}_{16}\text{O}$  ((moles of 1,2- $\text{C}_8\text{H}_{16}\text{O}$ )(W sites) $^{-1}$ ).

### 3. RESULTS AND DISCUSSION

**3.1. Nature of Supported  $\text{WO}_x$  on  $\gamma\text{-Al}_2\text{O}_3$ .** The series of  $X\text{-WO}_x\text{-Al}_2\text{O}_3$  samples synthesized that spans coverages from 0.03 to 0.9  $\text{W}\cdot\text{nm}^{-2}$  (and associated mass loadings, Table 1) is expected to form predominantly isolated  $\text{WO}_x$  complexes at the lowest coverages and oligomeric  $\text{WO}_x$  species at the greatest coverages.  $\gamma\text{-Al}_2\text{O}_3$  was selected as a support in order to stabilize  $\text{WO}_x$  complexes and suppress metal loss to the liquid phase during catalysis<sup>34</sup> and also because alumina does not catalyze epoxidation or oxidative cleavage reactions. The electronic, coordinative, and crystallographic structures of  $\text{WO}_x$  complexes over  $\gamma\text{-Al}_2\text{O}_3$  depend upon the coverage of W atoms ( $\text{W}\cdot\text{nm}^{-2}$ ) as shown by systematic changes in the band gap energies determined by DRUV-vis, the evolution of Raman features related to  $\text{W}=\text{O}$  and  $\text{W}-\text{O}-\text{W}$  coordination, and diffraction peaks apparent in XRD.

Figure 1 shows that the band gap energy increases as the surface coverage of  $\text{WO}_x$  decreases from 0.9 to 0.06  $\text{W}\cdot\text{nm}^{-2}$ ,

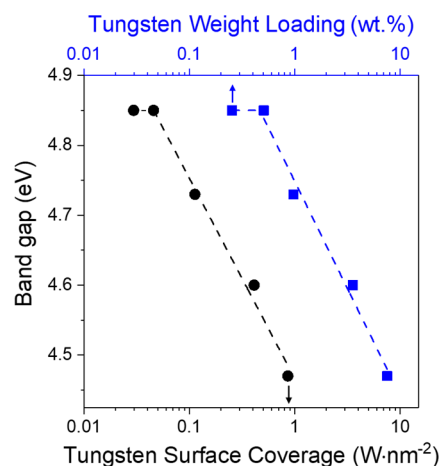


**Figure 1.** Band gap energies as a function of the surface coverage of W atoms ( $\text{W}\cdot\text{nm}^{-2}$ ) (bottom axis) and the weight loading of tungsten (top axis) on  $\gamma\text{-Al}_2\text{O}_3$ .

which indicates that the fraction of W atoms present at monomeric or small oligomeric  $\text{WO}_x$  units is greater at lower coverages on  $\gamma\text{-Al}_2\text{O}_3$ . The band gap reaches a value of  $\sim 4.85$  eV for  $X\text{-WO}_x\text{-Al}_2\text{O}_3$  samples with surface coverage equal to or less than 0.06  $\text{W}\cdot\text{nm}^{-2}$ . These band gaps are much greater than that for  $\text{WO}_3$  (2.8 eV)<sup>35</sup> and together with the change in band gap with coverage suggest that materials with W atom coverages below 0.06  $\text{W}\cdot\text{nm}^{-2}$  approach a constant distribution of  $\text{WO}_x$  complexes, which likely contains a significant fraction of W atoms in monomer or dimer species.

In situ Raman spectroscopy was used to assess the structure of the  $\text{WO}_x$  species on  $\gamma\text{-Al}_2\text{O}_3$  while in a dehydrated state and to determine these structures and also identify the reactive species formed by  $\text{H}_2\text{O}_2$  activation in solutions used for catalysis (0.5 M  $\text{H}_2\text{O}_2$ , 1.98 M  $\text{H}_2\text{O}$ ,  $\text{CH}_3\text{CN}$  solvent, 313 K). The  $\gamma\text{-Al}_2\text{O}_3$  support does not give rise to any features visible in the Raman spectra<sup>36</sup> (Figure S4), which demonstrates that all peaks observed in Figure 2 reflect vibrational modes that involve  $\text{WO}_x$ . Raman spectra of dehydrated 0.03- and 0.06- $\text{WO}_x\text{-Al}_2\text{O}_3$  samples contain a single detectable feature at 953  $\text{cm}^{-1}$  assigned to  $\nu(\text{W}=\text{O})$ ,<sup>37,38</sup> which signifies the presence

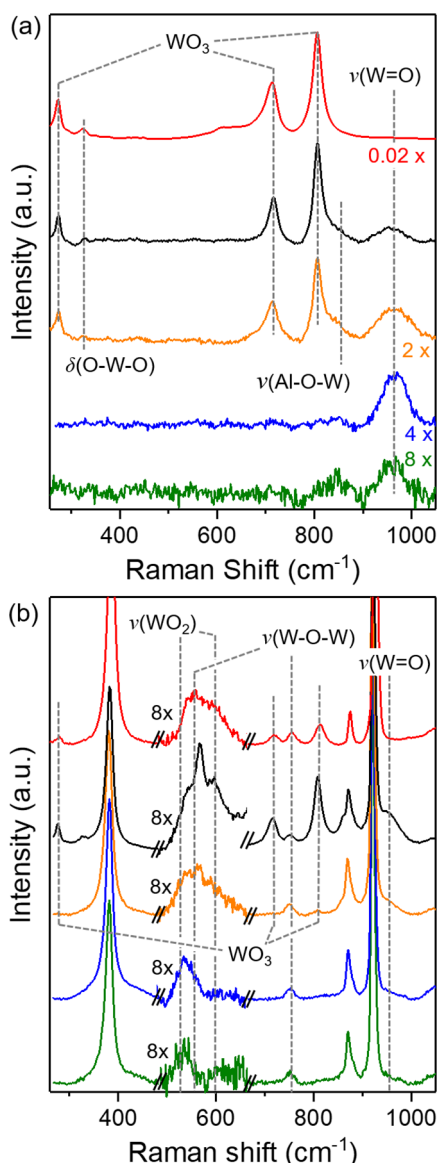


**Figure 2.** In situ Raman spectra of  $\text{WO}_x\text{-Al}_2\text{O}_3$  (0.03 (green line), 0.06 (blue line), 0.4 (orange line), and 0.9 (black line)  $\text{W}\cdot\text{nm}^{-2}$ ) and  $\text{WO}_3$  (red line) (a) under dry flowing helium (298 K, 101 kPa He) after dehydration (773 K, 1 h,  $20\text{ cm}^3\cdot\text{min}^{-1}$ ) and (b) within flowing solutions of  $\text{H}_2\text{O}_2$  and  $\text{CH}_3\text{CN}$  (0.5 M  $\text{H}_2\text{O}_2$ , 1.98 M  $\text{H}_2\text{O}$ , 313 K,  $1\text{ cm}^3\cdot\text{min}^{-1}$ ). Spectra are offset for clarity, and spectra obtained in the liquid phase are normalized using a feature of  $\text{CH}_3\text{CN}$  at  $920\text{ cm}^{-1}$ .

of distorted  $[\text{WO}_4]^{-2}$  monotungstate. In contrast, Raman spectra of  $\text{X}\text{-WO}_x\text{-Al}_2\text{O}_3$  materials with greater W atom coverages ( $\geq 0.4\text{ W}\cdot\text{nm}^{-2}$ ) possess this peak (i.e.,  $\nu(\text{W}=\text{O})$ ) but also exhibit Raman scattering features at 274, 719, and  $809\text{ cm}^{-1}$  that resemble  $\delta(\text{O}-\text{W}-\text{O})$ ,  $\nu(\text{W}-\text{O})$ , and  $\nu(\text{O}-\text{W}-\text{O})$  modes, respectively, of the monoclinic  $\text{WO}_3$  structure<sup>39</sup> that appear prominently in the spectra of  $\text{WO}_3$ . Finally, Raman bands at  $323$  and  $867\text{ cm}^{-1}$  correspond to the  $\delta(\text{O}-\text{W}-\text{O})$  and  $\nu(\text{W}-\text{O}-\text{Al})$  of dehydrated surface oligomeric  $\text{WO}_x$ , respectively. These findings suggest that dehydrated  $\text{WO}_x\text{-Al}_2\text{O}_3$  catalysts contain predominantly monomeric  $\text{WO}_x$  complexes at the lowest coverages and mixtures of oligomeric tungstate surface species and  $\text{WO}_3$  aggregates at surface coverages of  $0.4\text{ W}\cdot\text{nm}^{-2}$  and greater.

Figure 2b shows steady-state Raman spectra of the catalysts within solutions of  $\text{H}_2\text{O}_2$  and  $\text{CH}_3\text{CN}$  similar to those for kinetic measurements. All of these spectra contain strong Raman bands at  $380$  and  $920\text{ nm}^{-1}$  from  $\text{CH}_3\text{CN}$  (e.g.,  $\delta(\text{C}\equiv\text{N})$  and  $\nu(\text{C}-\text{C})$ , respectively)<sup>40</sup> and a peak at  $879\text{ cm}^{-1}$  that corresponds to  $\nu(\text{O}-\text{O})$  of liquid-phase  $\text{H}_2\text{O}_2$ .<sup>41</sup> In situ Raman spectra of all  $\text{X}\text{-WO}_x\text{-Al}_2\text{O}_3$  catalysts exhibit peaks at  $520$ ,  $556$ ,  $750$ ,  $953$ , and  $600\text{ cm}^{-1}$  that correspond to  $\nu_s(\text{WO}_2)$ ,<sup>42,43</sup>  $\nu_s(\text{W}-\text{O}-\text{W})$ ,<sup>44</sup>  $\nu_{\text{as}}(\text{W}-\text{O}-\text{W})$ ,<sup>44</sup>  $\nu(\text{W}=\text{O})$ ,<sup>37,38</sup> and  $\nu_{\text{as}}(\text{WO}_2)$ <sup>42,43</sup> modes, respectively. The W-peroxo complexes (i.e.,  $\text{W}-(\eta^2\text{-O}_2)$ ,  $520$  and  $600\text{ cm}^{-1}$ ) will be described in detail later (Section 3.2). Features for  $\nu(\text{W}-\text{O}-\text{W})$  appear in aqueous  $\text{H}_2\text{O}_2$  solution even at the lowest W atom coverages ( $\leq 0.06\text{ W}\cdot\text{nm}^{-2}$ ) despite the absence of this peak on the dehydrated materials. Wachs et al. examined  $\text{WO}_x\text{-Al}_2\text{O}_3$  materials with a similar range of surface coverage ( $0.5\text{--}4.5\text{ W}\cdot\text{nm}^{-2}$ ) using a combination of Raman, DRUV-vis, and XANES analysis to determine the structure of  $\text{WO}_x$  complexes in the presence and absence of coordinated water molecules.<sup>35,45</sup> Analysis of these results concluded that hydration of  $\text{WO}_x$  induces mobility and permits dimerization and formation of  $\text{W}-\text{O}-\text{W}$  linkages observable by Raman.<sup>45</sup> Comparisons between Raman spectra (Figure 2) and measured band gaps (Figure 1) suggest, therefore, that these  $\text{X}\text{-WO}_x\text{-Al}_2\text{O}_3$  materials with W atom coverages equal to and less than  $0.06\text{ W}\cdot\text{nm}^{-2}$  contain primarily  $\text{WO}_x$  monomers when dehydrated but form a noticeable fraction of dimer complexes under the reaction conditions. The Raman spectra of the hydrated  $\text{X}\text{-WO}_x\text{-Al}_2\text{O}_3$  materials with high W coverages ( $\geq 0.4\text{ W}\cdot\text{nm}^{-2}$ ) show the same peaks found on those under dehydrated conditions.

X-ray diffractograms confirm the presence of crystalline  $\text{WO}_3$  particles on  $\text{WO}_x\text{-Al}_2\text{O}_3$  samples with greater W atom coverages (Figure S5). All  $\text{X}\text{-WO}_x\text{-Al}_2\text{O}_3$  materials give diffraction features that correspond to  $\gamma\text{-Al}_2\text{O}_3$  (JCPDS No. 29-0063); however, the  $0.9\text{-WO}_x\text{-Al}_2\text{O}_3$  catalyst exhibits additional weak XRD peaks that match those for crystalline  $\text{WO}_3$  (JCPDS No. 83-950). These diffraction features were absent from all catalysts with W atom surface coverages less than  $0.9\text{ W}\cdot\text{nm}^{-2}$ , which suggests that the Raman features reminiscent of  $\text{WO}_3$  on  $0.4\text{-WO}_x\text{-Al}_2\text{O}_3$  reflect poorly ordered  $\text{WO}_3$  oligomers. Taken together, the results from DRUV-vis, in situ Raman, and XRD strongly suggest that samples with the lowest W atom surface coverages ( $\leq 0.06\text{ W}\cdot\text{nm}^{-2}$ ) stabilize predominantly monomeric and dimeric  $\text{WO}_x$  complexes under catalytic conditions. Significant fractions of W atoms reside as  $\text{WO}_x$  oligomers at surface coverages between  $0.06$  and  $0.4\text{ W}\cdot\text{nm}^{-2}$ , and crystalline  $\text{WO}_3$  nanoparticles also form at greater W atom coverages. Consequently, we compare reactive intermediates, chemical interrogation of active sites, and rates of oxidative cleavage between  $0.06\text{-WO}_x\text{-Al}_2\text{O}_3$  (designated hereafter as  $\text{WO}_x\text{-Al}_2\text{O}_3$ ) and  $\text{WO}_3$  to understand how differences between the coordination and structure of  $\text{WO}_x$  complexes affect the surface chemistry relevant for oxidative cleavage reactions.

**3.2. Reactive Intermediates Derived from  $\text{H}_2\text{O}_2$ .** As discussed in the previous section (Section 3.1), Figure 2b shows representative Raman spectra of  $\text{X}\text{-WO}_x\text{-Al}_2\text{O}_3$  and  $\text{WO}_3$  in contact with a solution of  $\text{H}_2\text{O}_2$  in  $\text{CH}_3\text{CN}$  (0.5 M  $\text{H}_2\text{O}_2$ , 1.98 M  $\text{H}_2\text{O}$ ,  $\text{CH}_3\text{CN}$  solvent, 313 K). All of these Raman spectra contain vibrational features at  $\sim 520$  and  $\sim 600\text{ cm}^{-1}$ , which correspond to the  $\nu_s(\text{WO}_2)$  and  $\nu_{\text{as}}(\text{WO}_2)$  modes, respectively.<sup>42,43</sup> Interpretation of the Raman spectra in Figure

2 suggests that  $\text{WO}_x$  complexes initially possess oxo groups ( $\text{W}=\text{O}$ ), form  $\text{W}-(\eta^2\text{-O}_2)$  species on contact with  $\text{H}_2\text{O}_2$ , and likely return to their initial state following the consumption of  $\text{W}-(\eta^2\text{-O}_2)$  species.

The  $\text{H}_2\text{O}_2$ -derived complexes on W-containing catalysts include  $\text{W}-(\eta^2\text{-O}_2)$  and W-hydroperoxo ( $\text{W}-\text{OOH}$ ),<sup>46</sup> and while  $\text{W}-\text{OOH}$  and other metal-hydroperoxos do not appear to possess Raman active vibrational modes,<sup>47,48</sup> these species provide distinguishable peaks in UV-vis spectroscopy that reflect the ligand to metal charge transfer (LMCT) energies of the complexes. Figure 3a shows steady-state UV-vis spectra of  $\gamma\text{-Al}_2\text{O}_3$ ,  $\text{WO}_x\text{-Al}_2\text{O}_3$ , and  $\text{WO}_3$  while within the same

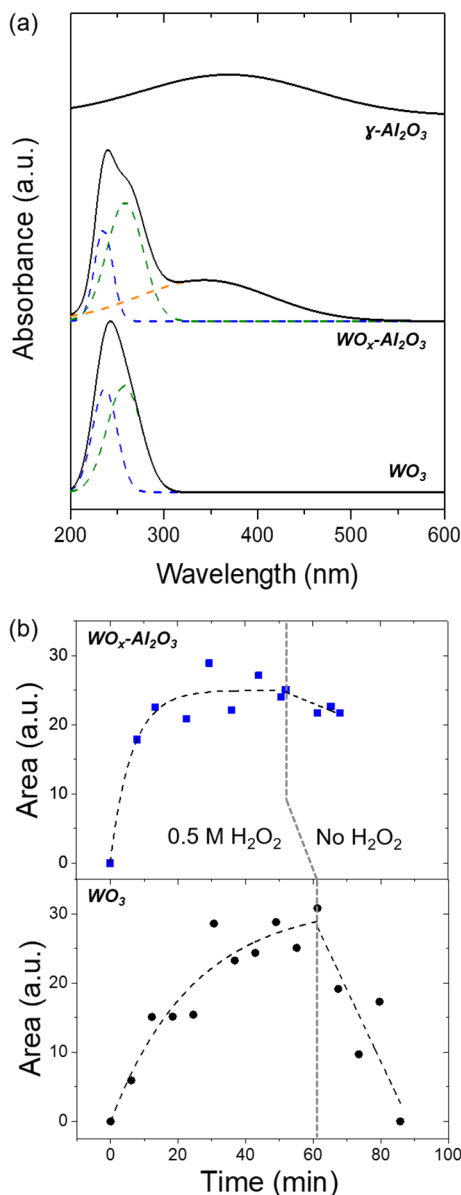


**Figure 3.** (a) UV-vis spectra of  $\text{H}_2\text{O}_2$  activated  $\gamma\text{-Al}_2\text{O}_3$ , 0.06- $\text{WO}_x\text{-Al}_2\text{O}_3$ , and  $\text{WO}_3$  acquired in situ within flowing  $\text{H}_2\text{O}_2$  solution (0.5 M  $\text{H}_2\text{O}_2$ , 1.98 M  $\text{H}_2\text{O}$ , 313 K,  $1\text{ cm}^3\text{-min}^{-1}$ ). Spectra are offset and normalized by the maximum absorbance value. (b) Coverages of  $\text{H}_2\text{O}_2$ -derived intermediates (determined from UV-vis peak areas) as a function of time for  $\text{WO}_x\text{-Al}_2\text{O}_3$  and  $\text{WO}_3$ . Background spectrum was obtained in  $\text{CH}_3\text{CN}$  (1.98 M  $\text{H}_2\text{O}$ , 313 K) before time is equal to zero.

solution (0.5 M  $\text{H}_2\text{O}_2$ ,  $\text{CH}_3\text{CN}$ , 313 K). These spectra reveal absorbance features from 200 to 300 nm, which reflect the presence of  $\text{W}-(\eta^2\text{-O}_2)$  and  $\text{W}-\text{OOH}$  species for both  $\text{WO}_x\text{-Al}_2\text{O}_3$  and  $\text{WO}_3$  catalysts.<sup>49,50</sup> Spectral deconvolution of the features indicates two bands at  $\sim 230$  and  $\sim 255$  nm; the lower energy features are known to correspond to  $\text{M}-\text{OOH}$ , while the higher energy peaks are assigned to the  $\text{M}-(\eta^2\text{-O}_2)$  for  $\text{H}_2\text{O}_2$ -activated metal oxide catalyst.<sup>27,47,51,52</sup> The broad band near 345 nm on  $\text{WO}_x\text{-Al}_2\text{O}_3$  resembles a similar feature on bare  $\gamma\text{-Al}_2\text{O}_3$  after contact with aqueous  $\text{H}_2\text{O}_2$  and therefore corresponds to a  $\text{H}_2\text{O}_2$ -derived species on the alumina support. These spectra show that both  $\text{WO}_x\text{-Al}_2\text{O}_3$  and  $\text{WO}_3$  catalysts possess  $\text{W}-(\eta^2\text{-O}_2)$  and  $\text{W}-\text{OOH}$  after  $\text{H}_2\text{O}_2$  activation; however,  $\text{WO}_x\text{-Al}_2\text{O}_3$  seems to stabilize a greater ratio of  $\text{W}-\text{OOH}$  to  $\text{W}-(\eta^2\text{-O}_2)$  than  $\text{WO}_3$ , perhaps due to a greater local concentration of protons derived from Brønsted acid sites on the support.<sup>47</sup>

These in situ UV-vis spectra provide the means to examine the reversibility of  $\text{H}_2\text{O}_2$  activation over W atoms on the catalysts examined here (Figure 3b). First, the catalysts were exposed to a  $\text{H}_2\text{O}_2$  solution (0.5 M  $\text{H}_2\text{O}_2$ , 1.98 M  $\text{H}_2\text{O}$ ,  $\text{CH}_3\text{CN}$   $1\text{ mL}\cdot\text{min}^{-1}$ ) to establish steady-state coverages of  $\text{W}-(\eta^2\text{-O}_2)$  and  $\text{W}-\text{OOH}$  species at 313 K. Once the absorbance features become constant, the flowing solution was replaced with a pure  $\text{CH}_3\text{CN}$  solution ( $1\text{ mL}\cdot\text{min}^{-1}$ ) that did not contain  $\text{H}_2\text{O}$  and  $\text{H}_2\text{O}_2$  and intensities of the absorbance features were monitored. The results indicate that  $\text{W}-(\eta^2\text{-O}_2)$  and  $\text{W}-\text{OOH}$  species form slowly ( $\sim 1$  h) and desorb (or decompose) within 0.4 h on  $\text{WO}_3$ . In comparison, the coverage of  $\text{H}_2\text{O}_2$ -derived intermediates saturates within 10 min on  $\text{WO}_x\text{-Al}_2\text{O}_3$ , and the coverage of the  $\text{W}-(\eta^2\text{-O}_2)$  and  $\text{W}-\text{OOH}$  species remains nearly constant within pure  $\text{CH}_3\text{CN}$ . These results suggest that the  $\text{H}_2\text{O}_2$ -derived intermediates form irreversibly on  $\text{WO}_x\text{-Al}_2\text{O}_3$  but reversibly on  $\text{WO}_3$  on these time scales.

### 3.3. Titrations of Active Sites for Oxidative Cleavage.

Accurate comparisons between the different forms of tungsten oxide catalysts require direct measurement of the number of active sites, which should be conducted during catalytic reactions. Phenyl phosphonic acid (PPA) and other phosphonic acids can be used for this purpose, because these species deprotonate and the conjugate base binds to Lewis acidic transition metal atoms and inhibits catalytic turnovers.<sup>53</sup> Figure 4 shows that the oxidative cleavage rate decreases as the ratio of phenyl phosphonic acid to the total number of W atoms increases over both  $\text{WO}_3$  and  $\text{WO}_x\text{-Al}_2\text{O}_3$  catalysts. While these rates decrease systematically, addition of PPA does not completely suppress catalysis on either material. The residual catalytic rates may be caused by two effects. First, the steric hindrance provided by PPA may reduce turnover rates significantly for titrated W sites; however, these sites may still possess a fraction of their catalytic reactivity.<sup>27</sup> Second, PPA may bind reversibly to a fraction of the active sites, and therefore, reactants may still bind to and react with a fraction of sites that remain free of PPA.<sup>53,54</sup>

A linear extrapolation of these measurements at low coverages (Figure 4) provides an estimated for the number of active sites per gram of material. Figure 4a shows that this occurs when values of  $n_{\text{PPA}}(n_{\text{WO}_3})^{-1}$  approach  $(3.9 \pm 0.1) \times 10^{-3}$ , which corresponds to an active site density of  $17\ \mu\text{mol}\cdot\text{g}^{-1}$  of catalyst. In comparison, titrations of the  $\text{WO}_x\text{-Al}_2\text{O}_3$  catalyst show oxidative cleavage rates near zero at  $n_{\text{PPA}}(n_{\text{WO}_3})^{-1}$  values of  $1.02 \pm 0.14$ , indicating a site density

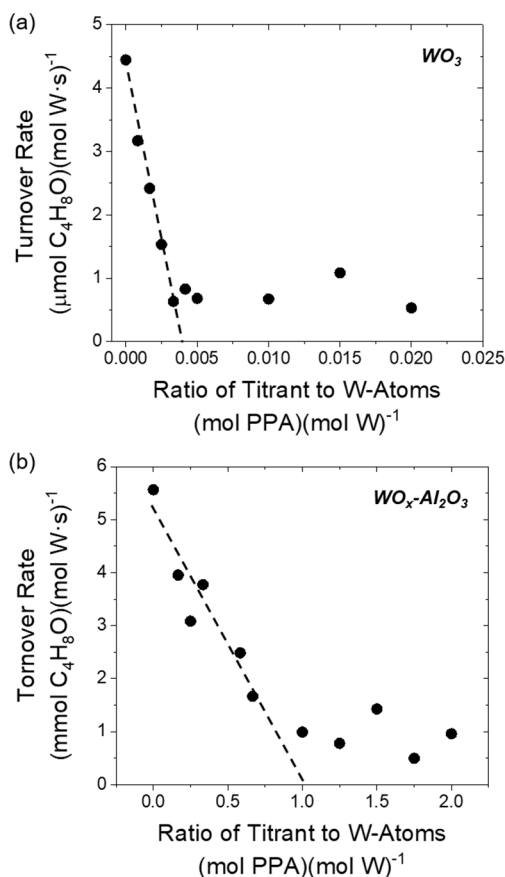


**Figure 4.** Turnover rates for oxidative cleavage of 4-octene (0.025 M 4-octene, 0.1 M  $H_2O_2$ , 333 K) as a function of  $n_{PPA}/n_W$  for (a)  $WO_3$  and (b)  $WO_x-Al_2O_3$ . Lines represent linear fits.

of  $28 \mu\text{mol}\cdot\text{g}^{-1}$  of total catalyst (Figure 4b). These results show, perhaps surprisingly, that the density of the active sites on the  $WO_x-Al_2O_3$  catalysts can surpass those on pure  $WO_3$  despite extremely low surface coverages of W atoms on the  $\gamma-Al_2O_3$  support. These differences originate from both the low surface area of the  $WO_3$  (Section 2.2) and the fact that only small fractions of the exposed W atoms on  $WO_3$  are catalytically active. The surface densities of W atoms on monoclinic  $WO_3$  are 7.3, 6.9, and 7.1 W atoms·nm<sup>-2</sup> for the (001), (100), and (010) facets, respectively.<sup>55</sup> Yet, the surface density of the active sites on  $WO_3$  is 1.09 sites·nm<sup>-2</sup>, as determined from the combination of PPA titrations and  $N_2$  physisorption measurements. These results indicate that only ~15% of all surface W atoms of  $WO_3$  are active for oxidative cleavage of 4- $C_8H_{16}$  with  $H_2O_2$ . In comparison, the surface density of the W atoms of  $WO_x-Al_2O_3$  is 0.06 W atoms·nm<sup>-2</sup>, and nearly all W atoms catalyze steps for oxidative cleavage (i.e., ~0.06 sites·nm<sup>-2</sup>). This finding, along with the analysis of in situ Raman spectra (Figure 2b), suggests that the active sites include a combination of oligomeric and monomeric tungsten

species. Notably, the surface density of the W atoms on  $\gamma-Al_2O_3$  can be increased to larger values while maintaining a high dispersion of these sites (Figures 1 and 2).

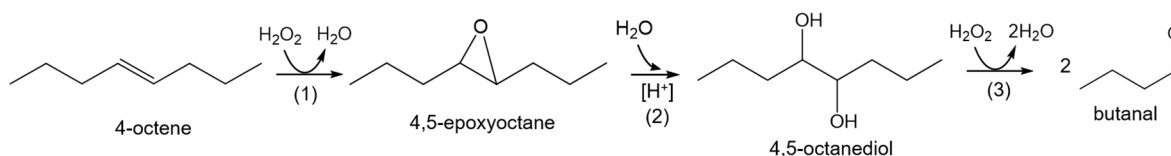
The greater number of active sites per gram of catalyst not only represents one advantage of the supported catalyst over  $WO_3$  but also in later comparisons of turnover rates and activation enthalpies demonstrate that the  $WO_x$  complexes on  $\gamma-Al_2O_3$  provide more favorable kinetics for the oxidative cleavage than  $WO_3$ .

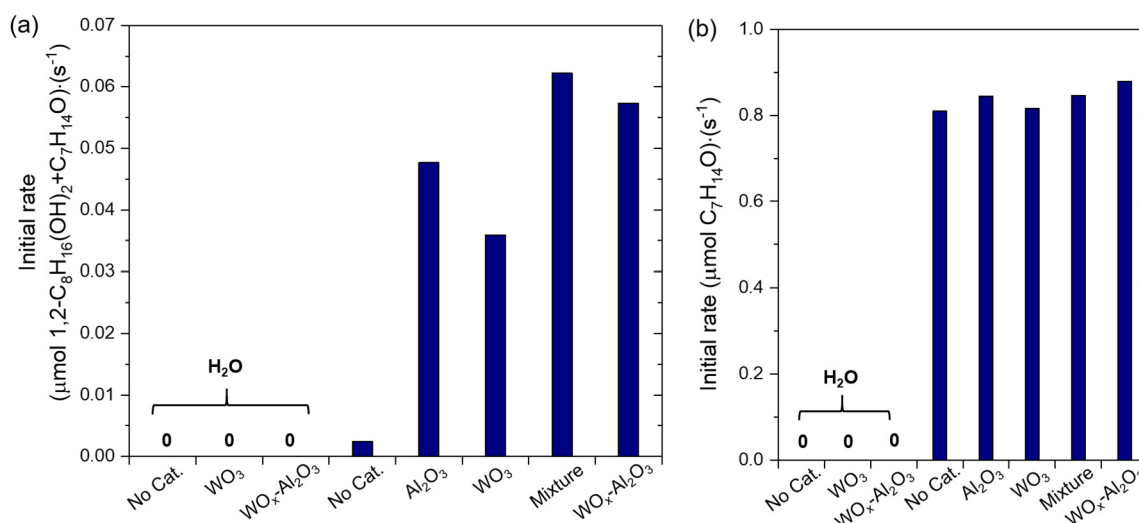
**3.4. Reaction Pathways and Site Requirements for Oxidative Cleavage of 4-Octene.** Scheme 2 shows individual balanced reactions that lead to the oxidative cleavage of 4-octene and includes the Lewis acid-catalyzed epoxidation of 4-octene by reaction with  $H_2O_2$ , Brønsted acid-catalyzed hydrolysis of 4,5-epoxyoctane to yield 4,5-octanediol, and C–C bond cleavage of 4,5-octanediol to form two equivalents of butanal, potentially through an alpha-hydroxy ketone intermediate as described by Venturello et al.<sup>56</sup> The initial epoxidation of 4-octene occurs readily on  $WO_3$  and  $WO_x-Al_2O_3$  catalysts in the presence of  $H_2O_2$  and requires both a solid catalyst and the oxidant, which agrees with previous investigations of epoxidation reactions with tungsten and other transition metal silicates.<sup>13,23,27,47,51</sup> In comparison, the role of the solid catalyst in the subsequent steps that convert the epoxide to the aldehydes is less clear. The initial rates for the hydrolysis and C–C bond cleavage steps (Scheme 2) were measured in the absence of a catalyst and also in the presence of  $WO_x-Al_2O_3$ ,  $WO_3$ ,  $\gamma-Al_2O_3$ , and a physical mixture of  $WO_3$  and  $\gamma-Al_2O_3$  to determine the active site requirements for these two steps. 1,2-Epoxyoctane and 1,2-octanediol were used as surrogates for the intermediates derived from 4-octene because these molecules were not available in high purities.

Figure 5a shows that rates for 1,2-epoxyoctane hydrolysis (determined as the summed rate of formation of the diol and the corresponding aldehydes) are immeasurably small over  $WO_x-Al_2O_3$  and  $WO_3$  and without a catalyst present in the absence of  $H_2O_2$  (1.98 M  $H_2O$ ,  $CH_3CN$ , 313 K). Rates become detectable in the presence of  $H_2O_2$  alone and increase significantly upon addition of either tungsten catalyst or the bare  $\gamma-Al_2O_3$  support (30 mg of each used). The acid-catalyzed hydrolysis rate is 60% greater over  $WO_x-Al_2O_3$  than that over  $WO_3$  (for an equal number of active W atoms), and the physical mixture of  $\gamma-Al_2O_3$  and  $WO_3$  shows hydrolysis rates comparable to  $WO_x-Al_2O_3$ . These observations indicate that  $H_2O_2$ -derived protic intermediates on  $\gamma-Al_2O_3$  or  $WO_x$  complexes (e.g.,  $W-OOH$ ) are responsible for epoxide hydrolysis and that the Brønsted acid sites intrinsic to these surfaces cannot facilitate these reactions in the absence of  $H_2O_2$ .

Figure 5b presents comparisons between the rates for the oxidative cleavage of 1,2-octanediol. The rate measured for the oxidative cleavage does not depend on the presence of any of the solid catalysts examined here. However, this reaction does require the presence of  $H_2O_2$ . These results suggest that C–C

#### Scheme 2. Oxidative Cleavage Process of 4-Octene





**Figure 5.** Initial rates for (a) acid-catalyzed hydrolysis of 1,2-epoxyoctane (steps 2 and 3 in Scheme 2; 0.025 M 1,2- $C_8H_{16}O$ , 0.1 or 0 M  $H_2O_2$ , 0.39 M  $H_2O$  in  $CH_3CN$  at 333 K) and (b) cleavage of the C–C bond of 1,2-octanediol (step 3 in Scheme 2; 0.025 M 1,2- $C_8H_{16}(OH)_2$ , 0.1 or 0 M  $H_2O_2$ , 0.39 M  $H_2O$  in  $CH_3CN$  at 333 K) in the absence of catalyst and over  $\gamma$ - $Al_2O_3$ ,  $WO_3$ , physical mixture of  $\gamma$ - $Al_2O_3$  and  $WO_3$ , and 0.06- $WO_x$ - $Al_2O_3$ . All reactions that involved tungstate catalysts used identical numbers of active sites (0.8  $\mu$ mol).

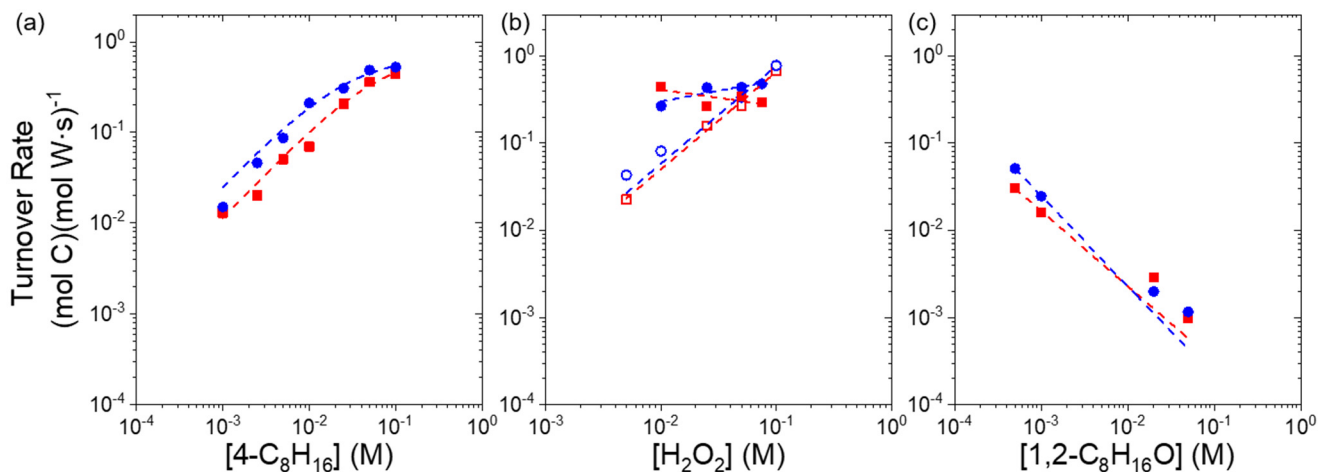


**Figure 6.** Turnover rates for oxidative cleavage of 4-octene (butanal formation) as a function of (a)  $[4-C_8H_{16}]$  for  $WO_3$  (red solid squares, 0.1 M  $H_2O_2$ , 0.39 M  $H_2O$ ) and  $WO_x-Al_2O_3$  (blue solid circles, 0.1 M  $H_2O_2$ , 0.39 M  $H_2O$ ), (b)  $[H_2O_2]$  for  $WO_3$  (red solid squares, 25 mM 4- $C_8H_{16}$ ; red open squares, 0.1 M 4- $C_8H_{16}$ ) and  $WO_x-Al_2O_3$  (blue solid circles, 25 mM 4- $C_8H_{16}$ ; blue open circles, 0.1 M 4- $C_8H_{16}$ ), and (c)  $[1,2-C_8H_{16}O]$  for  $WO_3$  (red solid squares 0.1 M 4- $C_8H_{16}$ , 0.1 M  $H_2O_2$ , 0.39 M  $H_2O$ ) and  $WO_x-Al_2O_3$  (blue solid circles, 0.1 M 4- $C_8H_{16}$ , 0.1 M  $H_2O_2$ , 0.39 M  $H_2O$ ) at 333 K.

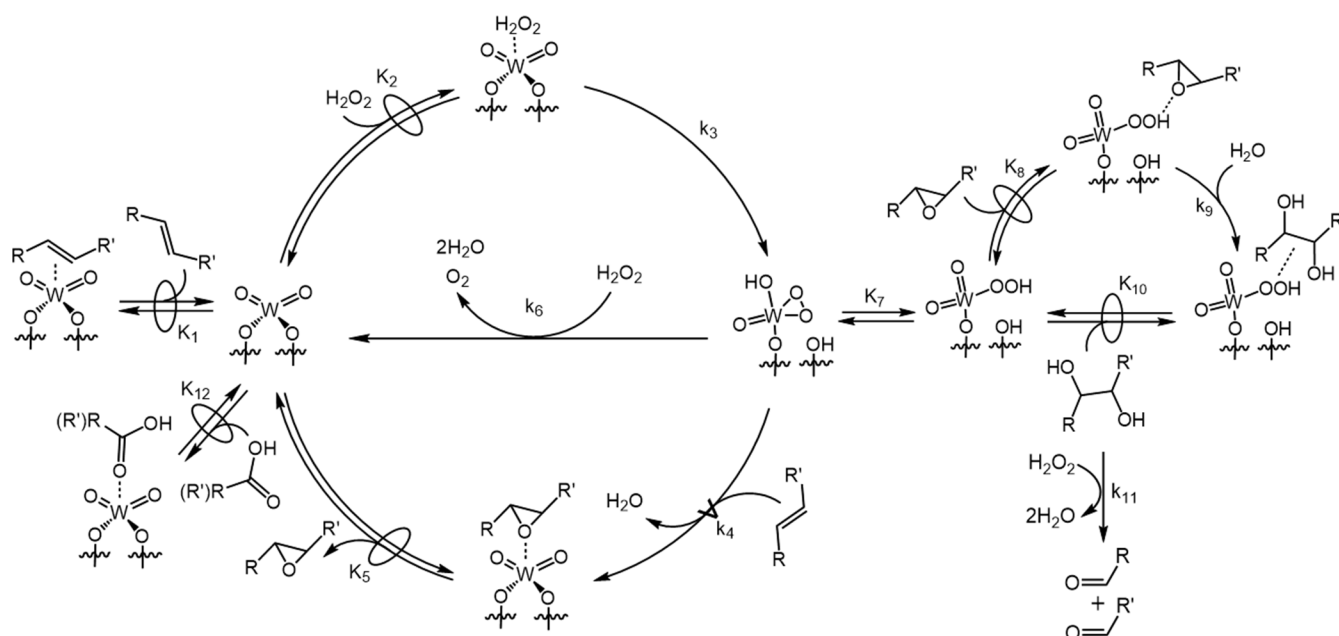
bond cleavage occurs by a homogeneous reaction (or series of reactions) with  $H_2O_2$  in aqueous  $CH_3CN$ , which agrees with proposals by Venturello et al.,<sup>56</sup> who described the oxidative cleavage of 1,2-octanediol via the formation of an unstable hydroperoxide adduct by nucleophilic attack of  $H_2O_2$  to the alpha-hydroxy ketone and subsequent decomposition to yield water and aldehyde products. Here, we postulate that the  $CH_3CN$  solvent may assist in this chemistry by deprotonating the diol in the absence of a solid catalyst.

The comparisons shown in Figure 5 demonstrate that multiple forms of catalytic sites participate in this reaction sequence; however, we demonstrate that the initial epoxidation of the alkene represents the kinetically relevant step (vide infra). Therefore, the structures of the  $WO_x$  complexes that form the active sites for this chemistry have a dominant role in determining the overall rate of this reaction.

**3.5. Turnover Rates and Rate Expressions for Oxidative Cleavage of 4-Octene.** Rates for oxidative cleavage ( $r_{OC}$ ) of 4-octene over  $WO_x-Al_2O_3$  and  $WO_3$  catalysts depend on the concentrations of the organic reactant, the oxidant, and the products because these concentrations determine the coverage of surface intermediates formed during catalysis. Figure 6 shows turnover rates (determined using site counts from PPA titrations in Section 3.3) for the formation of butanal ( $C_4H_8O$ ) by oxidative cleavage of 4-octene as a function of concentrations of 4-octene ( $[4-C_8H_{16}]$ , where brackets denote the concentration of a species), hydrogen peroxide ( $[H_2O_2]$ ), and 1,2-epoxyoctane ( $[1,2-C_8H_{16}O]$ , as a surrogate for 4,5- $C_8H_{16}O$ , which was not available at sufficient purities). Turnover rates of butanal formation ( $(\text{mol C})(\text{mol W}\cdot\text{s})^{-1}$ ) were used to report oxidative cleavage rates.

Turnover rates for oxidative cleavage of 4- $C_8H_{16}$  increase linearly with  $[4-C_8H_{16}]$  at lower concentrations (less than 50

**Scheme 3. Proposed Mechanism for Oxidative Cleavage of Alkene and Unsaturated Fatty Acids with H<sub>2</sub>O<sub>2</sub> over Tungsten Oxide Catalysts<sup>a</sup>**



<sup>a</sup>The double arrow with a circle symbol denotes a quasi-equilibrated step, and the forward arrow with an upside down V symbol signifies the kinetically relevant step for the formation of oxidative cleavage products.

mM 4-C<sub>8</sub>H<sub>16</sub>) and become nearly constant at greater values of [4-C<sub>8</sub>H<sub>16</sub>] (0.05–0.1 M 4-C<sub>8</sub>H<sub>16</sub>, Figure 6a) for both WO<sub>x</sub>-Al<sub>2</sub>O<sub>3</sub> and WO<sub>3</sub> catalysts. At low ratios of [4-C<sub>8</sub>H<sub>16</sub>] to [H<sub>2</sub>O<sub>2</sub>], turnover rates depend linearly on [4-C<sub>8</sub>H<sub>16</sub>] (Figure 6a) but do not depend on [H<sub>2</sub>O<sub>2</sub>] (Figure 6b), which suggests that active sites are covered by H<sub>2</sub>O<sub>2</sub>-derived reactive intermediates (i.e., W-(η<sup>2</sup>-O<sub>2</sub>) and W-OOH). Furthermore, turnover rates for butanal formation do not change appreciably as a function of [H<sub>2</sub>O] (Figure S10), which shows that interactions between H<sub>2</sub>O and active intermediates or active sites remain constant across the range of concentrations examined (0.39–4.0 M H<sub>2</sub>O). At relatively high ratios of [4-C<sub>8</sub>H<sub>16</sub>] to [H<sub>2</sub>O<sub>2</sub>], turnover rates are independent of [4-C<sub>8</sub>H<sub>16</sub>] (Figure 6a), proportional to [H<sub>2</sub>O<sub>2</sub>] (Figure 6b), and inversely proportional to [1,2-C<sub>8</sub>H<sub>16</sub>O] (Figure 6c), which indicates that the MARI becomes a 4-C<sub>8</sub>H<sub>16</sub>-derived species (e.g., 4,5-C<sub>8</sub>H<sub>16</sub>O) at these larger [4-C<sub>8</sub>H<sub>16</sub>].

Scheme 3 shows a series of steps that are consistent with the rate measurements for 4-octene conversion (Figure 6) and the site requirements determined for hydrolysis of the epoxide and oxidative cleavage of the diol (Figure 5). The catalytic cycle involves the quasi-equilibrated adsorption of 4-C<sub>8</sub>H<sub>16</sub> (step 1) and H<sub>2</sub>O<sub>2</sub> (step 2). H<sub>2</sub>O<sub>2</sub> activates on WO<sub>3</sub> and WO<sub>x</sub>-Al<sub>2</sub>O<sub>3</sub> to form W-(η<sup>2</sup>-O<sub>2</sub>) and W-OOH, and this process appears to be partially reversible on time scales of ~0.5 h, as shown by in situ UV-vis measurements (Figure 3). The turnover rates for butanal formation, however, are significantly faster (5–170 times) than rates for H<sub>2</sub>O<sub>2</sub> desorption, which indicates that H<sub>2</sub>O<sub>2</sub> activates irreversibly on both WO<sub>3</sub> and WO<sub>x</sub>-Al<sub>2</sub>O<sub>3</sub> during reactions with alkenes. Subsequently, the W-(η<sup>2</sup>-O<sub>2</sub>) complexes<sup>26–28</sup> react with 4-C<sub>8</sub>H<sub>16</sub> to form 4,5-epoxyoctane (step 4) or with a second molecule of H<sub>2</sub>O<sub>2</sub> to decompose into water and oxygen molecules (step 6). The selectivities for the consumption of H<sub>2</sub>O<sub>2</sub> by epoxidation (step 4) or by H<sub>2</sub>O<sub>2</sub> decomposition (step 6) depend on the concentrations of 4-

C<sub>8</sub>H<sub>16</sub> and H<sub>2</sub>O<sub>2</sub>: the ratios of the rates for these two pathways are proportional to the ratio of [4-C<sub>8</sub>H<sub>16</sub>] to [H<sub>2</sub>O<sub>2</sub>] (Section S5.2). 4,5-Epoxyoctane desorbs in a quasi-equilibrated manner (step 5). We propose that acidic W-OOH complexes form reversibly from W-(η<sup>2</sup>-O<sub>2</sub>) (step 7), and these Brønsted acids protonate and bind the epoxide (step 8). Subsequently, the protonated intermediate reacts with water to irreversibly hydrolyze the epoxide and form 4,5-epoxyoctanediol (step 9), which desorbs (step 10). Finally, a closed series of steps converts 4,5-epoxyoctanediol to an alpha-hydroxy ketone intermediate by reaction with the basic solvent and then cleaves the C–C bonds following nucleophilic attack of H<sub>2</sub>O<sub>2</sub> in the liquid phase (step 11).<sup>25,36</sup> These processes (step 11) must occur homogeneously within the solvent because rates for the oxidative cleavage of diols remain constant in the absence or presence of any of the catalysts examined here (Figure 5b).

Changes in the concentrations of the fluid-phase intermediates and products of the reaction sequence (Scheme 2) as a function of time (Figures S6 and S7) show that the selectivities toward 4,5-epoxyhexane remain small (≤5%) in comparison to butanal selectivities (>95%). These comparisons suggest that the rates of steps 9 and 11 exceed that for step 4 by a significant amount, which implies an even greater difference between the associated rate constants (i.e.,  $k_9, k_{11} \gg k_4$ ). Consequently, we propose that the epoxidation of 4-octene represents the kinetically relevant step that determines the rates of oxidative cleavage ( $r_{OC}$ )

$$r_{OC} = k_4[4-C_8H_{16}][W-OO] \quad (3)$$

where  $k_4$  is the rate constant for step 4 and [W-OO] is the number of H<sub>2</sub>O<sub>2</sub>-derived reactive intermediates (sum of [W-(η<sup>2</sup>-O<sub>2</sub>)] and [W-OOH]). Application of the pseudo-steady-state hypothesis to [W-OO] (Section S5.1) leads to eq 4

$$\frac{r_{\text{OC}}}{[L]} = \frac{k_3 k_4 K_2 [4\text{-C}_8\text{H}_{16}] [\text{H}_2\text{O}_2]}{k_4 [4\text{-C}_8\text{H}_{16}] + k_6 [\text{H}_2\text{O}_2]} \beta \quad (4)$$

where  $k_i$  and  $K_i$  are the rate constant and the equilibrium constant, respectively, for step  $i$  and  $[L]$  is the total number of active sites, as measured by PPA titrations. The denominator of eq 4 contains the term  $\beta$ , which represents a balance on the species that occupy the active site as

$$\beta = 1 + K_1 [4\text{-C}_8\text{H}_{16}] + K_2 [\text{H}_2\text{O}_2] + \frac{k_3 K_2 [\text{H}_2\text{O}_2]}{k_4 [4\text{-C}_8\text{H}_{16}] + k_6 [\text{H}_2\text{O}_2]} + \frac{[4, 5\text{-C}_8\text{H}_{16}\text{O}]}{K_5} \quad (5)$$

where the five terms signify the numbers of sites that are occupied by  $\text{CH}_3\text{CN}$ ,  $4\text{-C}_8\text{H}_{16}$ ,  $\text{H}_2\text{O}_2$ ,  $\text{W}-(\eta^2\text{-O}_2)$  and  $\text{W-OOH}$ , and  $4,5\text{-C}_8\text{H}_{16}\text{O}$ , respectively.

The complete form of the rate expression (eq 4) takes a simpler form when the active sites are assumed to be covered primarily by the  $\text{W-OO}$  species derived from  $\text{H}_2\text{O}_2$  and the epoxide product. Equation 4 becomes

$$\frac{r_{\text{OC}}}{[L]} = \frac{\frac{k_3 k_4 K_2 [4\text{-C}_8\text{H}_{16}] [\text{H}_2\text{O}_2]}{k_4 [4\text{-C}_8\text{H}_{16}] + k_6 [\text{H}_2\text{O}_2]}}{\frac{k_3 K_2 [\text{H}_2\text{O}_2]}{k_4 [4\text{-C}_8\text{H}_{16}] + k_6 [\text{H}_2\text{O}_2]} + \frac{[4, 5\text{-C}_8\text{H}_{16}\text{O}]}{K_5}} \quad (6)$$

which recognizes that the coverage of the  $\text{W-OO}$  species depends on rates of steps 3, 4, and 6. The variations between the turnover rates on  $\text{WO}_3$  and on  $\text{WO}_x\text{-Al}_2\text{O}_3$  may reflect changes in the barriers and energetics of multiple elementary steps, which obviates clear interpretations of the key reasons for these differences. However, the pool of  $\text{W}-(\eta^2\text{-O}_2)$  and  $\text{W-OOH}$  formed by  $\text{H}_2\text{O}_2$  activation becomes the MARI at the lowest  $[4\text{-C}_8\text{H}_{16}]$ , which causes eq 6 to collapse to a common form

$$\frac{r_{\text{OC}}}{[L]} = k_4 [4\text{-C}_8\text{H}_{16}] \quad (7)$$

This result matches the experimental turnover rates that increase in proportion to  $[4\text{-C}_8\text{H}_{16}]$  (Figure 6a) and remain constant with  $[\text{H}_2\text{O}_2]$  (Figure 6b). Equation 7 shows that differences among turnover rates for oxidative cleavage on  $\text{WO}_3$  and  $\text{WO}_x\text{-Al}_2\text{O}_3$  catalysts can be attributed to values of  $k_4$  and to intrinsic activation barriers for this single step when  $\text{W}-(\eta^2\text{-O}_2)$  and  $\text{W-OOH}$  saturate active sites.

When concentrations of  $4\text{-C}_8\text{H}_{16}$  exceed that of  $\text{H}_2\text{O}_2$  over  $\text{WO}_3$ , the epoxide product ( $4,5\text{-C}_8\text{H}_{16}\text{O}$ ) becomes the MARI (as inferred from Figure 6c). When this coincides with rates for epoxidation that exceed those for  $\text{H}_2\text{O}_2$  decomposition, eq 6 takes the form

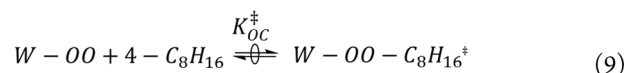
$$\frac{r_{\text{OC}}}{[L]} = \frac{k_3 K_2 K_5 [\text{H}_2\text{O}_2]}{[4, 5\text{-C}_8\text{H}_{16}\text{O}]} \quad (8)$$

Equation 8 is quantitatively consistent with turnover rates that do not depend on  $[4\text{-C}_8\text{H}_{16}]$  (Figure 6a) but do increase with  $[\text{H}_2\text{O}_2]$  (Figure 6b). This rate expression also predicts turnover rates that possess an inverse first-order dependence on the concentration of epoxides, which agrees with the results shown in Figure 6c (here, rates are depicted as a function of  $1,2\text{-C}_8\text{H}_{16}\text{O}$  because  $4,5\text{-C}_8\text{H}_{16}\text{O}$  was not available).

The spectroscopic and catalytic results presented (vide supra) suggest that the reaction pathways responsible for the oxidative cleavage are identical on  $\text{WO}_3$  and  $\text{WO}_x\text{-Al}_2\text{O}_3$

catalysts, as are the rate expressions. Turnover rates for the oxidative cleavage of 4-octene, however, are  $\sim 75\%$  greater over  $\text{WO}_x\text{-Al}_2\text{O}_3$  than those over  $\text{WO}_3$  at identical kinetic regimes. The reason for this difference is described below (Section 3.6).

**3.6. Effects of W Site Structure on Turnover Rates for Oxidative Cleavage.** The reference state and the transition state for oxidative cleavage can be theoretically be related by the transition-state theory (TST).<sup>57</sup> The apparent activation enthalpies can be used to compare the relative stability of the transition states over two different catalysts. TST proposed that  $\text{W-OO}$  ( $\text{W}-(\eta^2\text{-O}_2)$  and  $\text{W-OOH}$ ) and gaseous  $4\text{-C}_8\text{H}_{16}$  exist in equilibrium with the transition state ( $\text{W-OO-C}_8\text{H}_{16}$ ) for the elementary step (step 4 in Scheme 3), which is expressed as follows



where  $K_{\text{OC}}^{\ddagger}$  is the transition state equilibrium constant for the rate-determining step of the oxidative cleavage process. Restating the rate expression for the oxidative cleavage in terms of the number of transition states yields the following

$$\frac{r_{\text{OC}}}{[L]} = \frac{k_{\text{B}} T}{h} [\text{W-OO-C}_8\text{H}_{16}^{\ddagger}] \quad (10)$$

where  $T$  is the temperature in Kelvin and  $k_{\text{B}}$  and  $h$  are Boltzmann's and Planck's constants, respectively. When the reaction rates are measured with  $\text{W-OO}$  as the MARI, this equation can be re-expressed as follows

$$\frac{r_{\text{OC}}}{[L]} = \frac{k_{\text{B}} T}{h} K_{\text{OC}}^{\ddagger} [4\text{-C}_8\text{H}_{16}] \quad (11)$$

From this equation,  $K_{\text{OC}}^{\ddagger}$  can be determined by measurement of TOR at a given temperature. The activation enthalpy can be also determined by regression of the measured  $K_{\text{OC}}^{\ddagger}$  as a function of inverse temperature, because  $K_{\text{OC}}^{\ddagger}$  can be expressed in terms of  $\Delta H_{\text{OC}}^{\ddagger}$  and  $\Delta S_{\text{OC}}^{\ddagger}$  as follows

$$K_{\text{OC}}^{\ddagger} = e^{(-\Delta H_{\text{OC}}^{\ddagger}/RT + \Delta S_{\text{OC}}^{\ddagger}/R)} \quad (12)$$

where  $R$  is the ideal gas constant.  $\Delta H_{\text{OC}}^{\ddagger}$  values for  $\text{WO}_3$  and  $\text{WO}_x\text{-Al}_2\text{O}_3$  catalysts were determined from Figure S13.  $\Delta H_{\text{OC}}^{\ddagger}$  over  $\text{WO}_x\text{-Al}_2\text{O}_3$  ( $36 \pm 3 \text{ kJ}\cdot\text{mol}^{-1}$ ) is  $\sim 24 \text{ kJ}\cdot\text{mol}^{-1}$  lower than that over  $\text{WO}_3$  ( $60 \pm 6 \text{ kJ}\cdot\text{mol}^{-1}$ ), which suggests that differences in the electronic structure of catalytically  $\text{W}$  active sites supported on  $\gamma\text{-Al}_2\text{O}_3$  enthalpically favor epoxidation and subsequent oxidative cleavage of 4-octene by a significant margin.

Linear free-energy relationships provide a quantitative relationship between the chemical reactivity of a complex and its structure.<sup>58,59</sup> Noticeably, formation of the transition state structure for 4-octene epoxidation (i.e., the kinetically relevant process for oxidative cleavage) reproduces many of the changes in the coordinative structure of the active site and the surrounding solvent molecules as does adsorption of 1,2-epoxyoctane, an available mimic (Scheme S2). The enthalpy of adsorption for 1,2-epoxyoctane ( $\Delta H_{\text{Ads,epox}}$ ) onto the  $\text{W}$  sites of both catalysts was measured by isothermal titration calorimetry (Figure 7). The value of  $\Delta H_{\text{Ads,epox}}$  for  $\text{WO}_x\text{-Al}_2\text{O}_3$  is  $-93 \pm 1 \text{ kJ}\cdot\text{mol}^{-1}$ , and that on  $\text{WO}_3$  is  $-48 \pm 1 \text{ kJ}\cdot\text{mol}^{-1}$ , which shows that the epoxide binds  $45 \text{ kJ}\cdot\text{mol}^{-1}$  more exothermically to the isolated  $\text{WO}_x$  complexes on  $\gamma\text{-Al}_2\text{O}_3$  in comparison to sites upon crystalline  $\text{WO}_3$ . These results suggest that the isolated  $\text{WO}_x$  complexes possess greater Lewis

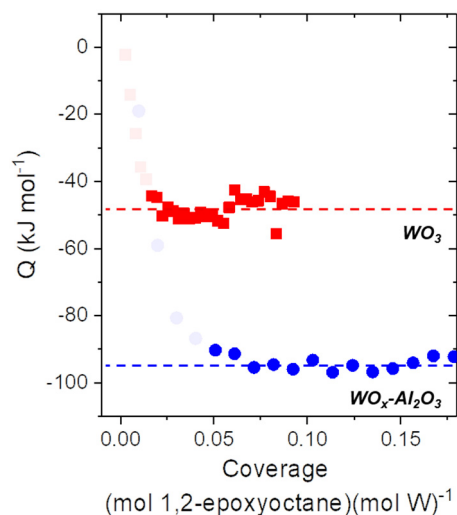


**Figure 7.** Heat released for 1,2-epoxyoctane binding to  $\text{WO}_3$  and  $\text{WO}_x\text{-Al}_2\text{O}_3$  in  $\text{CH}_3\text{CN}$  at 298 K as a function of 1,2-epoxyoctane coverage.

acid strength. Moreover, Table 2 compares values for  $\Delta H_{\text{Ads,epox}}$  and  $\Delta H_{\text{OC}}^\ddagger$  and demonstrates that the enthalpic

**Table 2. Apparent Activation Enthalpies ( $\Delta H_{\text{OC}}^\ddagger$ ) for Oxidative Cleavage of 4-Octene and Adsorption Enthalpies of 1,2-Epoxyoctane ( $\Delta H_{\text{Ads,epox}}$ ) on  $\text{WO}_x\text{-Al}_2\text{O}_3$  and  $\text{WO}_3$  Catalysts**

catalyst	$\Delta H_{\text{OC}}^\ddagger$ <sup>a</sup> (kJ·mol <sup>-1</sup> )	$\Delta H_{\text{Ads,epox}}$ <sup>b</sup> (kJ·mol <sup>-1</sup> )
$\text{WO}_3$	60 ± 6	-48 ± 1
$\text{WO}_x\text{-Al}_2\text{O}_3$	36 ± 3	-93 ± 1

<sup>a</sup>Measured under conditions in which  $\text{W}-(\eta^2\text{-O}_2)$  and  $\text{W}-\text{OOH}$  saturate W active sites (0.01 M 4- $\text{C}_8\text{H}_{16}\text{O}$ , 0.1 M  $\text{H}_2\text{O}_2$ ). <sup>b</sup>Measured by isothermal titration calorimetry.

stabilization of the epoxidation transition state correlates with the exothermicity of epoxide adsorption to the active site and

exhibits a transfer coefficient ( $\alpha$ , constant describing the proportionality between the activation enthalpy and the heat of adsorption) of  $\sim 0.5$ .

**3.7. Rates of Oxidative Cleavage of Oleic Acid with  $\text{H}_2\text{O}_2$ .** Reactions of oleic acid with  $\text{H}_2\text{O}_2$  over these tungstate catalysts show time-dependent changes in the concentrations of the fluid-phase species (Figure S8) that differ significantly from the types of products formed during consumption of 4-octene over two  $\text{WO}_3$  and  $\text{WO}_x\text{-Al}_2\text{O}_3$  catalysts. On  $\text{WO}_3$ , the epoxide forms with high selectivities ( $\sim 99\%$ ) and subsequent steps occur at incredibly low rates. In contrast,  $\text{WO}_x\text{-Al}_2\text{O}_3$  gives high initial selectivities to the epoxide, but these values decrease exponentially over time due to secondary ring-opening and oxidative cleavage steps that form the corresponding aldehydes and carboxylic acid products. We measured the initial turnover rates for oleic acid consumption ( $-r_{\text{OA}}$ , the combined rates of formation of epoxide, aldehyde, and acid products) over both catalysts as a function of  $[\text{OA}]$ ,  $[\text{H}_2\text{O}_2]$ , and  $[1,2\text{-C}_8\text{H}_{16}\text{O}]$  (a surrogate for the epoxide of OA). The observations and forms of the resulting rate expression qualitatively agree with measurements for the reactions of 4-octene with  $\text{H}_2\text{O}_2$  over these same catalysts, which indicates that the mechanisms and elementary involved are similar (Scheme 3).

Initial turnover rates for oleic acid consumption ( $-r_{\text{OA}}/[\text{L}]$ ) over  $\text{WO}_3$  and  $\text{WO}_x\text{-Al}_2\text{O}_3$  depend linearly on  $[\text{OA}]$  at the lowest concentrations and approach a sublinear dependence at higher  $[\text{OA}]$  (Figure 8a). At low ratios of  $[\text{OA}]$  to  $[\text{H}_2\text{O}_2]$ , turnover rates on  $\text{WO}_3$  and  $\text{WO}_x\text{-Al}_2\text{O}_3$  increase with  $[\text{OA}]$  and depend weakly on  $[\text{H}_2\text{O}_2]$  and  $[1,2\text{-C}_8\text{H}_{16}\text{O}]$ . However, higher  $[\text{OA}]$  to  $[\text{H}_2\text{O}_2]$  ratios show rates that increase with a clearly sublinear dependence upon  $[\text{OA}]$  and a stronger positive dependence on  $[\text{H}_2\text{O}_2]$  for both catalysts. When  $[\text{OA}]$  and  $[\text{H}_2\text{O}_2]$  have similar values, two noticeable differences between  $\text{WO}_3$  and  $\text{WO}_x\text{-Al}_2\text{O}_3$  appear. Turnover rates on  $\text{WO}_x\text{-Al}_2\text{O}_3$  show a greater positive dependence on  $[\text{H}_2\text{O}_2]$  values and a stronger inverse dependence on  $[1,2\text{-C}_8\text{H}_{16}\text{O}]$  in comparison to  $\text{WO}_3$  at identical conditions. These observations have the general form of the rate expression presented for

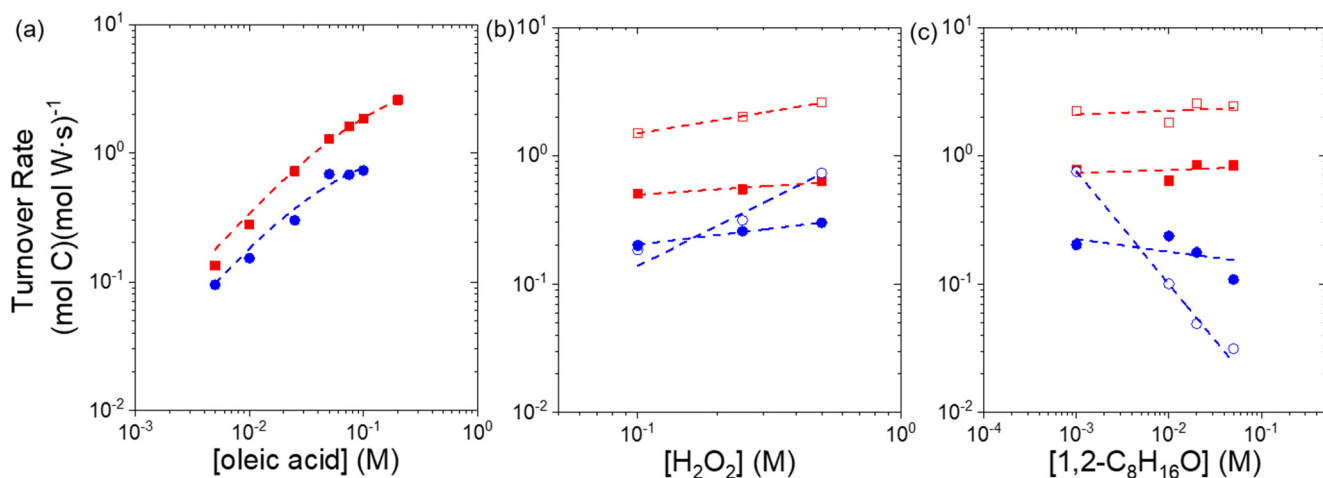


**Figure 8.** Turnover rates for the formation of epoxide, aldehyde, and acid products over  $\text{WO}_3$  and  $\text{WO}_x\text{-Al}_2\text{O}_3$  as a function of (a)  $[\text{oleic acid}]$  for  $\text{WO}_3$  (red solid squares, 0.5 M  $\text{H}_2\text{O}_2$ , 1.98 M  $\text{H}_2\text{O}$ ) and  $\text{WO}_x\text{-Al}_2\text{O}_3$  (blue solid circles, 0.5 M  $\text{H}_2\text{O}_2$ , 1.98 M  $\text{H}_2\text{O}$ ), (b)  $[\text{H}_2\text{O}_2]$  for  $\text{WO}_3$  (red solid squares, 50 mM oleic acid; red open squares, 0.1 M oleic acid) and  $\text{WO}_x\text{-Al}_2\text{O}_3$  (blue solid circles, 50 mM oleic acid; blue open circles, 0.1 M oleic acid), and (c)  $[1,2\text{-C}_8\text{H}_{16}\text{O}]$  for  $\text{WO}_3$  (red solid squares, 50 mM oleic acid, 0.5 M  $\text{H}_2\text{O}_2$ , 1.98 M  $\text{H}_2\text{O}$ ; red open squares, 0.1 M oleic acid, 0.5 M  $\text{H}_2\text{O}_2$ , 1.98 M  $\text{H}_2\text{O}$ ) and  $\text{WO}_x\text{-Al}_2\text{O}_3$  (blue solid circles, 50 mM oleic acid, 0.5 M  $\text{H}_2\text{O}_2$ , 1.98 M  $\text{H}_2\text{O}$ ; blue open circles, 0.1 M oleic acid, 0.5 M  $\text{H}_2\text{O}_2$ , 1.98 M  $\text{H}_2\text{O}$ ) at 343 K.

oxidative cleavage of 4-octene, which for oleic acid consumption takes the form

$$-r_{\text{OA}} = k_4[\text{OA}][\text{W}-\text{OO}] \quad (13)$$

where  $k_4$  is the rate constant for step 4 and  $[\text{W}-\text{OO}]$  is the number of  $\text{H}_2\text{O}_2$ -derived reactive intermediates (sum of  $[\text{W}-(\eta^2-\text{O}_2)]$  and  $[\text{W}-\text{OOH}]$ ). Application of the pseudo-steady-state hypothesis to  $[\text{W}-\text{OO}]$  (Section S3) leads to eq 14 for  $\text{WO}_3$  and  $\text{WO}_x-\text{Al}_2\text{O}_3$

$$\frac{-r_{\text{OA}}}{[\text{L}]} = \frac{k_3 k_4 K_2 [\text{OA}] [\text{H}_2\text{O}_2]}{k_4 [\text{OA}] + k_6 [\text{H}_2\text{O}_2]} \quad (14)$$

Here, the term  $\beta$  represents a balance on the species that occupy the active sites

$$\beta = 1 + \frac{k_3 K_2 [\text{H}_2\text{O}_2]}{k_4 [\text{OA}] + k_6 [\text{H}_2\text{O}_2]} + K_1 [\text{OA}] + K_2 [\text{H}_2\text{O}_2] + \frac{[\text{Epox}]}{K_5} + K_{12} [\text{NA}] + K_{12} [\text{AA}] \quad (15)$$

where the seven terms signify the numbers of sites that are occupied by  $\text{CH}_3\text{CN}$ ,  $\text{H}_2\text{O}_2$ -derived species ( $\text{W}-(\eta^2-\text{O}_2)$  and  $\text{W}-\text{OOH}$ ), oleic acid, hydrogen peroxide, 8-(3-octyloxiran-2-yl)octanoic acid (Epox), nonanoic acid, and azelaic acid. The complete rate expression (eq 14) takes a simpler form when sites become saturated with certain subsets of the intermediates considered above.

The findings presented in Figure 8 indicate that the dominant surface species on  $\text{WO}_3$  and  $\text{WO}_x-\text{Al}_2\text{O}_3$  differ across the range of concentrations examined. Rates over  $\text{WO}_3$  suggest that combinations of  $\text{W}-(\eta^2-\text{O}_2)$ ,  $\text{W}-\text{OOH}$ , and oleic acid saturate active, sites and the rate expression (eq 14) becomes

$$\frac{-r_{\text{OA}}}{[\text{L}]} = \frac{\frac{k_3 k_4 K_2 [\text{OA}] [\text{H}_2\text{O}_2]}{k_4 [\text{OA}] + k_6 [\text{H}_2\text{O}_2]}}{\frac{k_3 K_2 [\text{H}_2\text{O}_2]}{k_4 [\text{OA}] + k_6 [\text{H}_2\text{O}_2]} + K_1 [\text{OA}]} \quad (16)$$

Figure 8 and eq 16 suggest that oleic acid possesses a significant coverage at all reaction conditions on  $\text{WO}_3$  but yields a large fraction of the active sites to  $\text{W}-(\eta^2-\text{O}_2)$  and  $\text{W}-\text{OOH}$  at the greatest  $[\text{H}_2\text{O}_2]$  to  $[\text{OA}]$  ratios. The epoxide, in comparison, does not occupy a detectable number of sites. We attribute the difference between the apparent concentration dependencies seen for 4-octene (Figure 6) and oleic acid (Figure 8) to strong binding of the carboxylate to acidic W atoms, perhaps within a bidentate configuration.

Oleic acid consumption rates over  $\text{WO}_x-\text{Al}_2\text{O}_3$  exhibit apparent concentration dependencies that closely mimic those for 4-octene. This rate behavior can be reproduced by assuming that  $\text{W}-(\eta^2-\text{O}_2)$ ,  $\text{W}-\text{OOH}$ , and the epoxide cover active sites, such that a similar derivation and combination of assumptions cause eq 14 to become

$$\frac{-r_{\text{OA}}}{[\text{L}]} = \frac{\frac{k_3 k_4 K_2 [\text{OA}] [\text{H}_2\text{O}_2]}{k_4 [\text{OA}] + k_6 [\text{H}_2\text{O}_2]}}{\frac{k_3 K_2 [\text{H}_2\text{O}_2]}{k_4 [\text{OA}] + k_6 [\text{H}_2\text{O}_2]} + \frac{[\text{Epox}]}{K_5}} \quad (17)$$

Comparisons of the rate expressions for oleic acid consumption (eqs 16 and 17) suggest that the large difference in product selectivities between  $\text{WO}_3$  and  $\text{WO}_x-\text{Al}_2\text{O}_3$  originates from a much greater preference to bind oleic acid

relative to the epoxide on  $\text{WO}_3$ . The resulting high coverages of oleic acid on  $\text{WO}_3$  (a consequence of both concentration and equilibrium constants) appear to inhibit the rates at which the epoxide product binds to protic sites (step 8, Scheme 3) and undergoes hydrolysis (step 9, Scheme 3). Consequently, the selectivity toward the epoxide remains high on  $\text{WO}_3$  over the full range of reaction times (Figure S8c). The underlying reasons for this difference are not entirely clear. Measured  $\Delta H_{\text{Ads,epox}}$  values (Table 2) indicate that the sites on  $\text{WO}_x-\text{Al}_2\text{O}_3$  possess greater Lewis acid strength than those on  $\text{WO}_3$ , which seems at odds with the weaker binding of the carboxylate of oleic acid (i.e., the conjugate base). However, this discrepancy may allude to important features of the adsorption mode (e.g., bidentate or monodentate) that stabilize this adsorbate on an ordered surface of  $\text{WO}_3$  more so than on isolated  $\text{WO}_x$  on  $\gamma\text{-Al}_2\text{O}_3$ . Greater understanding of the cause for these differences will likely require the use of in situ infrared spectroscopy to examine the coordination of the organic reactive intermediates to W active sites.

#### 4. CONCLUSIONS

We synthesized a series of  $\gamma\text{-Al}_2\text{O}_3$ -supported tungstate catalysts with increasing W content via grafting methods to introduce isolated and oligomeric  $\text{WO}_x$  species on  $\gamma\text{-Al}_2\text{O}_3$ . While Raman results of dehydrated materials show large fractions of  $\text{WO}_x$  monomers, in situ Raman, DRUV-vis, and XRD results suggest that even the lowest W atom coverages lead to catalysts with mixtures of monomeric and dimeric  $\text{WO}_x$  species under the reaction conditions. Raman spectroscopy suggests that  $\text{W}=\text{O}$  intermediates exist prior to  $\text{H}_2\text{O}_2$  exposure, but these species do not react with the  $\text{C}=\text{C}$  bonds to form measurable quantities of products. Instead,  $\text{W}$ -peroxide complexes ( $\text{W}$ -peroxo ( $\text{W}-(\eta^2-\text{O}_2)$ )), formed by  $\text{H}_2\text{O}_2$  activation, react with alkenes to initiate steps that ultimately result in oxidative cleavage. The formation of  $\text{W}$ -peroxide complexes occurs irreversibly in the presence of alkene coreagents in  $\text{CH}_3\text{CN}$  solution because these complexes react to epoxidize the alkene much more quickly than they desorb.

Kinetic measurements show that  $\text{W}-(\eta^2-\text{O}_2)$  transfers O atoms to  $\text{C}=\text{C}$  bonds to form epoxides, and the epoxidation step is consistently a kinetically relevant step for 4-octene and oleic acid conversions with  $\text{H}_2\text{O}_2$ . Acidic  $\text{W}-\text{OOH}$  functions then protonate and hydrolyze the epoxide to form the diol, and subsequently, oxidative cleavage proceeds via a homogeneous reaction between an alpha-hydroxy ketone and  $\text{H}_2\text{O}_2$  in the liquid phase. The spectroscopic and catalytic results suggest that the reaction pathway responsible for oxidative cleavage is identical on  $\text{WO}_3$  and  $\text{WO}_x-\text{Al}_2\text{O}_3$  catalysts, as are the rate expressions. Turnover rates for oxidative cleavage of 4-octene, however, are 75% greater over  $\text{WO}_x-\text{Al}_2\text{O}_3$  than those over  $\text{WO}_3$  at identical kinetic regimes. The activation enthalpies for this reaction over  $\text{WO}_3$  and  $\text{WO}_x-\text{Al}_2\text{O}_3$  catalysts are  $60 \pm 6$  and  $36 \pm 3$   $\text{kJ}\cdot\text{mol}^{-1}$ , respectively. The differences between  $\Delta H^\ddagger$  on these catalysts correlate with differences in the Lewis acid strength of these active sites and their enthalpies of adsorption for the epoxide intermediate ( $\Delta H_{\text{Ads,epox}}$ ) as measured by isothermal titration calorimetry (ITC). These comparisons suggest that the isolated W sites give greater turnover rates, particularly at lower reaction temperatures, because alumina-supported  $\text{WO}_x$  species possess greater electronegativities, bind epoxide products more strongly, and

stabilize kinetically relevant transition states more effectively than W atoms exposed on WO<sub>3</sub>.

While the pathways and mechanisms for the oxidative cleavage of oleic acid resemble those for 4-octene oxidative cleavage, selectivities differ significantly over WO<sub>x</sub>-Al<sub>2</sub>O<sub>3</sub> and WO<sub>3</sub> catalysts. WO<sub>3</sub> mainly produces the 8-(3-octyloxiran-2-yl)octanoic acid (epoxide), while WO<sub>x</sub>-Al<sub>2</sub>O<sub>3</sub> gives high selectivities for oxidative cleavage products (i.e., acids and aldehydes). These differences reflect the limited number of protic sites and competitive adsorption of oleic acid to the W atoms on the WO<sub>3</sub> surface, which appears to prevent the epoxide from reacting with W-OOH complexes as required for hydrolysis.

These findings demonstrate that solid tungstate catalysts are effective materials for oxidative cleavage reactions: these materials give significant turnover rates for key elementary steps (e.g., H<sub>2</sub>O<sub>2</sub> activation, epoxidation, and diol hydrolysis). The form of the solid tungstate site (i.e., WO<sub>x</sub>) matters, however, because the oxide on which these active sites exist determines the effective electron affinity (i.e., Lewis acid strength), the barriers for epoxidation, and preferences to bind individual reactive intermediates. The supporting oxide also controls the number of protonated intermediates available to assist in the hydrolysis of the epoxide ring. Consequently, both turnover rates and product selectivities are sensitive to the surface that supports the WO<sub>x</sub> site. From a practical perspective, efforts to increase rates and selectivities must also consider the ability of the support to maintain the dispersion of WO<sub>x</sub> sites (i.e., suppress oligomerization and formation of WO<sub>3</sub> nanoparticles) and prevent dissolution of W atoms into the reactant solution. For these reasons, we expect that there are significant opportunities to further improve the performance of solid tungstate catalyst for H<sub>2</sub>O<sub>2</sub>-mediated oxidative cleavage reactions.

## ■ ASSOCIATED CONTENT

### Supporting Information

The Supporting Information is available free of charge at <https://pubs.acs.org/doi/10.1021/acscatal.0c05393>.

Results of hot filtration and recycle tests, diffuse-reflectance UV-vis, ex situ Raman, X-ray diffraction patterns, product concentrations and selectivities as a function of reaction time, effects of water concentrations on turnover rates, derivations of the rate expressions, and activation enthalpies and entropies for oxidative cleavage of 4-octene (PDF)

## ■ AUTHOR INFORMATION

### Corresponding Author

David W. Flaherty – DOE Center for Advanced Bioenergy and Bioproducts Innovation, University of Illinois at Urbana-Champaign, Urbana, Illinois 61801, United States; Department of Chemical and Biomolecular Engineering, University of Illinois at Urbana-Champaign, Urbana, Illinois 61801, United States; [orcid.org/0000-0002-0567-8481](https://orcid.org/0000-0002-0567-8481); Email: [dwfhlrty@illinois.edu](mailto:dwfhlrty@illinois.edu)

### Authors

Danim Yun – DOE Center for Advanced Bioenergy and Bioproducts Innovation, University of Illinois at Urbana-Champaign, Urbana, Illinois 61801, United States; Department of Chemical and Biomolecular Engineering,

University of Illinois at Urbana-Champaign, Urbana, Illinois 61801, United States; [orcid.org/0000-0001-9035-0351](https://orcid.org/0000-0001-9035-0351)

E. Zeynep Ayla – Department of Chemical and Biomolecular Engineering, University of Illinois at Urbana-Champaign, Urbana, Illinois 61801, United States

Daniel T. Bregante – Department of Chemical and Biomolecular Engineering, University of Illinois at Urbana-Champaign, Urbana, Illinois 61801, United States; [orcid.org/0000-0003-2157-1286](https://orcid.org/0000-0003-2157-1286)

Complete contact information is available at: <https://pubs.acs.org/doi/10.1021/acscatal.0c05393>

## Notes

The authors declare no competing financial interest.

## ■ ACKNOWLEDGMENTS

This work was funded by the DOE Center for Advanced Bioenergy and Bioproducts Innovation (U.S. Department of Energy, Office of Science, Office of Biological and Environmental Research under Award Number DE-SC0018420). Any opinions, findings, and conclusions or recommendations expressed in this publication are those of the authors and do not necessarily reflect the views of the U.S. Department of Energy. E.Z.A. and D.T.B. were supported by the U.S. Army Research Office under grant number W911NF-18-1-0100.

## ■ REFERENCES

- (1) Spannring, P.; Bruijninx, P. C. A.; Weckhuysen, B. M.; Klein Gebbink, R. J. M. Transition metal-catalyzed oxidative double bond cleavage of simple and bio-derived alkenes and unsaturated fatty acids. *Catal. Sci. Technol.* **2014**, *4* (8), 2182–2209.
- (2) Godard, A.; De Caro, P.; Thiebaud-Roux, S.; Vedrenne, E.; Mouloungui, Z. New environmentally friendly oxidative scission of oleic acid into azelaic acid and pelargonic acid. *J. Am. Oil Chem. Soc.* **2013**, *90* (1), 133–140.
- (3) De Leon Izeppi, G. A.; Dubois, J.-L.; Balle, A.; Soutelo-Maria, A. Economic risk assessment using Monte Carlo simulation for the production of azelaic acid and pelargonic acid from vegetable oils. *Ind. Crops Prod.* **2020**, *150*, 112411.
- (4) Zimmermann, F.; Meux, E.; Mieloszynski, J.-L.; Lecuire, J.-M.; Oget, N. Ruthenium catalyzed oxidation without CCl<sub>4</sub> of oleic acid, other monoenoic fatty acids and alkenes. *Tetrahedron Lett.* **2005**, *46* (18), 3201–3203.
- (5) Johnson, R.; Fritz, E. *Fatty Acids in Industry: Processes, Properties, Derivatives*; Marcel Dekker, New York and Basel, 1988; p 327.
- (6) Nouredini, H.; Kanabur, M. Liquid-phase catalytic oxidation of unsaturated fatty acids. *J. Am. Oil Chem. Soc.* **1999**, *76* (3), 305–312.
- (7) Behr, A.; Tenhumberg, N.; Wintzer, A. Efficient ruthenium-catalyzed oxidative cleavage of methyl oleate with hydrogen peroxide as oxidant. *RSC Adv.* **2013**, *3* (1), 172–180.
- (8) Cousin, T.; Chatel, G.; Kardos, N.; Andrioletti, B.; Draye, M. Recent trends in the development of sustainable catalytic systems for the oxidative cleavage of cycloalkenes by hydrogen peroxide. *Catal. Sci. Technol.* **2019**, *9* (19), 5256–5278.
- (9) Spannring, P.; Yazerski, V.; Bruijninx, P. C. A.; Weckhuysen, B. M.; Klein Gebbink, R. J. M. Fe-Catalyzed One-Pot Oxidative Cleavage of Unsaturated Fatty Acids into Aldehydes with Hydrogen Peroxide and Sodium Periodate. *Chem. - Eur. J.* **2013**, *19* (44), 15012–15018.
- (10) Henry, J. R.; Weinreb, S. M. A convenient, mild method for oxidative cleavage of alkenes with Jones reagent/osmium tetroxide. *J. Org. Chem.* **1993**, *58* (17), 4745–4745.
- (11) Travis, B. R.; Narayan, R. S.; Borhan, B. Osmium tetroxide-promoted catalytic oxidative cleavage of olefins: an organometallic ozonolysis. *J. Am. Chem. Soc.* **2002**, *124* (15), 3824–3825.

- (12) Santacesaria, E.; Sorrentino, A.; Rainone, F.; Di Serio, M.; Speranza, F. Oxidative cleavage of the double bond of monoenic fatty chains in two steps: a new promising route to azelaic acid and other industrial products. *Ind. Eng. Chem. Res.* **2000**, *39* (8), 2766–2771.
- (13) Turnwald, S.; Lorier, M.; Wright, L.; Mucalo, M. Oleic acid oxidation using hydrogen peroxide in conjunction with transition metal catalysis. *J. Mater. Sci. Lett.* **1998**, *17* (15), 1305–1307.
- (14) Haimov, A.; Cohen, H.; Neumann, R. Alkylated Polyethyleneimine/Polyoxometalate Synzymes as Catalysts for the Oxidation of Hydrophobic Substrates in Water with Hydrogen Peroxide. *J. Am. Chem. Soc.* **2004**, *126* (38), 11762–11763.
- (15) de la Garza, L. C.; De Oliveira Vigier, K.; Chatel, G.; Moores, A. Amphiphilic dipyrindinium-phosphotungstate as an efficient and recyclable catalyst for triphasic fatty ester epoxidation and oxidative cleavage with hydrogen peroxide. *Green Chem.* **2017**, *19* (12), 2855–2862.
- (16) Berkowitz, L. M.; Rylander, P. N. Use of ruthenium tetroxide as a multi-purpose oxidant. *J. Am. Chem. Soc.* **1958**, *80* (24), 6682–6684.
- (17) Carlsen, P. H.; Katsuki, T.; Martin, V. S.; Sharpless, K. B. A greatly improved procedure for ruthenium tetroxide catalyzed oxidations of organic compounds. *J. Org. Chem.* **1981**, *46* (19), 3936–3938.
- (18) Torii, S.; Inokuchi, T.; Kondo, K. A facile procedure for oxidative cleavage of enolic olefins to the carbonyl compounds with ruthenium tetroxide (RuO<sub>4</sub>). *J. Org. Chem.* **1985**, *50* (24), 4980–4982.
- (19) Leffler, P. E.; Kazantzis, G. Tungsten. *Handbook on the Toxicology of Metals*; Elsevier: 2015; pp 1297–1306.
- (20) Salles, L.; Aubry, C.; Thouvenot, R.; Robert, F.; Doremieux-Morin, C.; Chottard, G.; Ledon, H.; Jeannin, Y.; Bregeault, J. M. 31P and 183W NMR Spectroscopic Evidence for Novel Peroxo Species in the “H3 [PW12O40]. cntdot. yH2O/H2O2” System. Synthesis and X-ray Structure of Tetrabutylammonium ( $\mu$ -Hydrogen phosphato) bis ( $\mu$ -peroxo) bis (oxoperoxotungstate)(2-): A Catalyst of Olefin Epoxidation in a Biphasic Medium. *Inorg. Chem.* **1994**, *33* (5), 871–878.
- (21) Griffith, W. Polyoxometallates as homogeneous catalysts for organic oxidations. *Transition Met. Chem.* **1991**, *16* (5), 548–552.
- (22) Oguchi, T.; Ura, T.; Ishii, Y.; Ogawa, M. Oxidative cleavage of olefins into carboxylic acids with hydrogen peroxide by tungstic acid. *Chem. Lett.* **1989**, *18* (5), 857–860.
- (23) Noyori, R.; Aoki, M.; Sato, K. Green oxidation with aqueous hydrogen peroxide. *Chem. Commun.* **2003**, No. 16, 1977–1986.
- (24) Li, X.; Choo Ping Syong, J.; Zhang, Y. Sodium stannate promoted double bond cleavage of oleic acid by hydrogen peroxide over a heterogeneous WO<sub>3</sub> catalyst. *Green Chem.* **2018**, *20* (15), 3619–3624.
- (25) Antonelli, E.; D'Aloisio, R.; Gambaro, M.; Fiorani, T.; Venturello, C. Efficient Oxidative Cleavage of Olefins to Carboxylic Acids with Hydrogen Peroxide Catalyzed by Methyltrioctylammonium Tetrakis(oxodiperoxotungsto)phosphate(3-) under Two-Phase Conditions. Synthetic Aspects and Investigation of the Reaction Course. *J. Org. Chem.* **1998**, *63* (21), 7190–7206.
- (26) Sheng, M. N.; Zajacek, J. Hydroperoxide oxidations catalyzed by metals. III. Epoxidation of dienes and olefins with functional groups. *J. Org. Chem.* **1970**, *35* (6), 1839–1843.
- (27) Ayla, E. Z.; Potts, D. S.; Bregante, D. T.; Flaherty, D. W. Alkene Epoxidations with H<sub>2</sub>O<sub>2</sub> over Groups 4–6 Metal-Substituted BEA Zeolites: Reactive Intermediates, Reaction Pathways, and Linear Free Energy Relationships. *ACS Catal.* **2021**, *11*, 139–154.
- (28) Conte, V.; Di Furia, F.; Moro, S. The versatile chemistry of peroxo complexes of vanadium, molybdenum and tungsten as oxidants of organic compounds. *J. Phys. Org. Chem.* **1996**, *9* (6), 329–336.
- (29) Hammond, C.; Straus, J.; Righettoni, M.; Pratsinis, S. E.; Hermans, I. Nanoparticulate Tungsten Oxide for Catalytic Epoxidations. *ACS Catal.* **2013**, *3* (3), 321–327.
- (30) Maschmeyer, T.; Rey, F.; Sankar, G.; Thomas, J. M. Heterogeneous catalysts obtained by grafting metallocene complexes onto mesoporous silica. *Nature* **1995**, *378* (6553), 159–162.
- (31) Kubelka, P.; Munk, F. A contribution to the optics of pigments. *Z. Technol. Phys.* **1931**, *12* (593), 193.
- (32) Tauc, J.; Grigorovici, R.; Vancu, A. Optical properties and electronic structure of amorphous germanium. *Phys. Status Solidi B* **1966**, *15* (2), 627–637.
- (33) Mott, N. F.; Davis, E. A. *Electronic processes in non-crystalline materials*, 2nd ed.; Clarendon Press: Oxford, 1979; p 497.
- (34) Guntida, A.; Suriye, K.; Panpranot, J.; Praserttham, P. Lewis acid transformation to Bronsted acid sites over supported tungsten oxide catalysts containing different surface WO<sub>x</sub> structures. *Catal. Today* **2020**, *358*, 354–369.
- (35) Ross-Medgaarden, E. I.; Wachs, I. E. Structural determination of bulk and surface tungsten oxides with UV–vis diffuse reflectance spectroscopy and raman spectroscopy. *J. Phys. Chem. C* **2007**, *111* (41), 15089–15099.
- (36) Wachs, I. E.; Roberts, C. A. Monitoring surface metal oxide catalytic active sites with Raman spectroscopy. *Chem. Soc. Rev.* **2010**, *39* (12), 5002–5017.
- (37) Maity, N.; Barman, S.; Minenkov, Y.; Ould-Chikh, S.; Abou-Hamad, E.; Ma, T.; Qureshi, Z. S.; Cavallo, L.; D'Elia, V.; Gates, B. C.; et al. A Silica-Supported Monoalkylated Tungsten Dioxo Complex Catalyst for Olefin Metathesis. *ACS Catal.* **2018**, *8* (4), 2715–2729.
- (38) Lee, E. L.; Wachs, I. E. In situ spectroscopic investigation of the molecular and electronic structures of SiO<sub>2</sub> supported surface metal oxides. *J. Phys. Chem. C* **2007**, *111* (39), 14410–14425.
- (39) Garcia-Sanchez, R. F.; Ahmido, T.; Casimir, D.; Baliga, S.; Misra, P. Thermal effects associated with the Raman spectroscopy of WO<sub>3</sub> gas-sensor materials. *J. Phys. Chem. A* **2013**, *117* (50), 13825–13831.
- (40) Neelakantan, P. Raman spectrum of acetonitrile. *Proc. - Indian Acad. Sci., Sect. A* **1964**, *60*, 422–424.
- (41) Moreno, T.; Moran Lopez, M.A.; Huerta Illera, I.; Piqueras, C.M.; Sanz Arranz, A.; Garcia Serna, J.; Cocero, M.J. Quantitative Raman determination of hydrogen peroxide using the solvent as internal standard: Online application in the direct synthesis of hydrogen peroxide. *Chem. Eng. J.* **2011**, *166* (3), 1061–1065.
- (42) Maniatakou, A.; Karaliota, S.; Mavri, M.; Raptopoulou, C.; Terzis, A.; Karaliota, A. Synthesis, characterization and crystal structure of novel mononuclear peroxotungsten (VI) complexes. Insulinomimetic activity of W (VI) and Nb (V) peroxo complexes. *J. Inorg. Biochem.* **2009**, *103* (5), 859–868.
- (43) Barrio, L.; Campos-Martín, J. M.; Fierro, J. L. Spectroscopic and DFT study of tungstic acid peroxocomplexes. *J. Phys. Chem. A* **2007**, *111* (11), 2166–2171.
- (44) Cozar, O.; Magdas, D.; Nasdala, L.; Ardelean, I.; Damian, G. Raman spectroscopic study of some lead phosphate glasses with tungsten ions. *J. Non-Cryst. Solids* **2006**, *352* (28–29), 3121–3125.
- (45) Horsley, J. A.; Wachs, I. E.; Brown, J. M.; Via, G. H.; Hardcastle, F. D. Structure of surface tungsten oxide species in the WO<sub>3</sub>/Al<sub>2</sub>O<sub>3</sub> supported oxide system from X-ray absorption near-edge spectroscopy and Raman spectroscopy. *J. Phys. Chem.* **1987**, *91*, 4014–4020.
- (46) Jin, P.; Wei, D.; Wen, Y.; Luo, M.; Wang, X.; Tang, M. A combined experimental and DFT study of active structures and self-cycle mechanisms of mononuclear tungsten peroxo complexes in oxidation reactions. *J. Mol. Struct.* **2011**, *992* (1), 19–26.
- (47) Bregante, D. T.; Thornburg, N. E.; Notestein, J. M.; Flaherty, D. W. Consequences of Confinement for Alkene Epoxidation with Hydrogen Peroxide on Highly Dispersed Group 4 and 5 Metal Oxide Catalysts. *ACS Catal.* **2018**, *8* (4), 2995–3010.
- (48) Bordiga, S.; Damin, A.; Bonino, F.; Ricchiardi, G.; Lamberti, C.; Zecchina, A. The Structure of the Peroxo Species in the TS-1 Catalyst as Investigated by Resonant Raman Spectroscopy. *Angew. Chem., Int. Ed.* **2002**, *41* (24), 4734–4737.
- (49) Kamata, K.; Kuzuya, S.; Uehara, K.; Yamaguchi, S.; Mizuno, N.  $\mu$ - $\eta$ 1:  $\eta$ 1-Peroxo-Bridged Dinuclear Peroxotungstate Catalytically

Active for Epoxidation of Olefins. *Inorg. Chem.* **2007**, *46* (9), 3768–3774.

(50) Das, N.; Chowdhury, S.; Purkayastha, R. N. D. Peroxo–tungstate (VI) complexes: syntheses, characterization, reactivity, and DFT studies. *Monatsh. Chem.* **2019**, *150* (7), 1255–1266.

(51) Bregante, D. T.; Flaherty, D. W. Periodic trends in olefin epoxidation over group IV and V framework-substituted zeolite catalysts: a kinetic and spectroscopic study. *J. Am. Chem. Soc.* **2017**, *139* (20), 6888–6898.

(52) Ziolk, M.; Sobczak, I.; Decyk, P.; Sobańska, K.; Pietrzyk, P.; Sojka, Z. Search for reactive intermediates in catalytic oxidation with hydrogen peroxide over amorphous niobium (V) and tantalum (V) oxides. *Appl. Catal., B* **2015**, *164*, 288–296.

(53) Eaton, T. R.; Boston, A. M.; Thompson, A. B.; Gray, K. A.; Notestein, J. M. Counting Active Sites on Titanium Oxide–Silica Catalysts for Hydrogen Peroxide Activation through In Situ Poisoning with Phenylphosphonic Acid. *ChemCatChem* **2014**, *6* (11), 3215–3222.

(54) Thornburg, N. E.; Nauert, S. L.; Thompson, A. B.; Notestein, J. M. Synthesis–Structure–Function Relationships of Silica-Supported Niobium(V) Catalysts for Alkene Epoxidation with H<sub>2</sub>O<sub>2</sub>. *ACS Catal.* **2016**, *6* (9), 6124–6134.

(55) Momma, K.; Izumi, F. VESTA 3 for three-dimensional visualization of crystal, volumetric and morphology data. *J. Appl. Crystallogr.* **2011**, *44* (6), 1272–1276.

(56) Venturello, C.; Ricci, M. Oxidative cleavage of 1, 2-diols to carboxylic acids by hydrogen peroxide. *J. Org. Chem.* **1986**, *51* (9), 1599–1602.

(57) Chorkendorff, I.; Niemantsverdriet, J. W. *Concepts of modern catalysis and kinetics*; John Wiley & Sons, 2017; p 107.

(58) Leveneur, S.; Murzin, D. Y.; Salmi, T. Application of linear free-energy relationships to perhydrolysis of different carboxylic acids over homogeneous and heterogeneous catalysts. *J. Mol. Catal. A: Chem.* **2009**, *303* (1), 148–155.

(59) van Santen, R. A.; Neurock, M.; Shetty, S. G. Reactivity Theory of Transition-Metal Surfaces: A Brønsted–Evans–Polanyi Linear Activation Energy–Free-Energy Analysis. *Chem. Rev.* **2010**, *110* (4), 2005–2048.